Structural basis of the neuronal M-current by an asymmetric KCNQ2/3 channel assembly

Xinyu Cheng[1,3,#], Shuangyan Wan[1,3,#], Dexiang Jiang[2,#], Hangyu Zhang[2,#], Bin Hu[4,#], Tong Che[1,3], Weiwei Nan[5], Zhuo Zhou[2], Chenxin Xiao[2], Ling Zhong[2], Yuting Zhang[5], Bo Yu[1,3], Ougen Liu[6], Jingjing Duan[7], Bing Xiong[8], Panpan Hou[2,9,*], Jin Zhang[1,3,*]

1 The MOE Basic Research and Innovation Center for the Targeted Therapeutics of Solid Tumors, School of Basic Medical Sciences, Jiangxi Medical College, Nanchang University, Nanchang, China; The Second Affiliated Hospital of Nanchang University, Nanchang, Jiangxi, China.

2 Dr. Neher's Biophysics Laboratory for Innovative Drug Discovery; State Key Laboratory of Mechanism and Quality of Chinese Medicine; & School of Pharmacy, Faculty of Medicine; Faculty of Chinese Medicine, Macau University of Science and Technology, Macau SAR, China.

3 Jiangxi Provincial Key Laboratory of Tumor Biology, School of Basic Medical Sciences, Jiangxi Medical College, Nanchang University, Nanchang, China.

4 School of Basic Medical Sciences, Gannan Medical University, Ganzhou, China.

5 Shenzhen Crystalo Biopharmaceutical Co., Ltd, Shenzhen, Guangdong 518118, China.

6 Department of Dermatology, The Second Affiliated Hospital of Nanchang University, Nanchang, Jiangxi, China.

7 Human Aging Research Institute (HARI), School of Life Sciences, Nanchang University, Nanchang, Jiangxi, 330031, China

8 Department of Medicinal Chemistry, Shanghai Institute of Materia Medica, Chinese Academy of Sciences, Shanghai 201203, China

9 Macau University of Science and Technology Innovation Technology Research Institute. Hengqin, Guangdong, China.

[#]These authors contributed equally.

[*]Corresponding authors.

E-mail addresses: pphou@must.edu.mo (Panpan Hou); zhangxiaokong@hotmail.com (Jin Zhang)

Abstract

The heteromeric KCNQ2/3 channel constitutes the molecular correlate of the neuronal M-current, a potassium conductance essential for stabilizing resting membrane potential and controlling neuronal excitability. Despite its physiological and therapeutic importance, the structural basis for its unique functional properties—distinct from homomeric KCNQ2 or KCNQ3—has remained enigmatic, and its definitive subunit stoichiometry has been a subject of long-standing debate. Here, leveraging a fusion protein strategy and multiple stoichiometry-sensitive pharmacological tools, we determined cryo-electron microscopy structures of the human KCNQ2/3 channel in both apo and drug-bound states, which unveil an asymmetric assembly with a predominant 1:3 (KCNQ2:KCNQ3) stoichiometry. This architectural principle underlies the M-channel's unique gating and pharmacology. Structural and functional analyses reveal that a reconfigured voltage-sensing domain and a pre-positioned C-terminal domain collectively lower the energy barrier for left-shifted voltage-dependent activation and enhanced PIP2 sensitivity. Furthermore, we elucidate the binding mechanism of the next-generation anticonvulsant XEN1101, demonstrating that its high selectivity for KCNQ2/3 arises from an optimized complementarity to the KCNQ3-dominated binding pocket within the heteromer. Our work resolves fundamental questions regarding the native architecture of the neuronal M-channel and establishes a structural foundation for the rational design of targeted therapies for epilepsy and related neurological disorders.

Introduction

Voltage-gated potassium channels of the KCNQ (Kv7) family (KCNQ1–5) play pivotal roles in regulating neuronal excitability, cardiac rhythm, and sensory signaling [1-6]. Among them, the KCNQ2/3 heteromer forms the molecular correlate of the neuronal M-current—a slowly activating, non-inactivating potassium current that stabilizes membrane potential and prevents hyperexcitability [7-10]. Disruption of this current, through mutations in KCNQ2 or KCNQ3, causes epileptic encephalopathies, and altered channel function has also been implicated in neuropathic pain and auditory disorders [11-24]. Despite its critical physiological importance, the molecular mechanism underlying M-current generation remains incompletely understood.

The M-current was first identified in sympathetic neurons more than four decades ago as a persistent, voltage-dependent potassium conductance that limits repetitive firing [25]. Molecular cloning later revealed KCNQ2 and KCNQ3 as its principal subunits, and co-expression of these channels reconstituted M-like currents in heterologous systems [7]. Homomeric KCNQ2 and KCNQ3 channels display markedly different gating behaviors, membrane trafficking efficiencies, and PIP_2 sensitivities, yet their heteromeric combination yields a robust and finely tuned current [26-30]. These findings imply that M-current properties arise from emergent structural features unique to the heteromeric complex—features that cannot be predicted from either subunit alone. However, despite extensive biochemical and electrophysiological studies, the exact subunit stoichiometry and assembly architecture of the KCNQ2/3 complex have long remained controversial. Early biochemical analyses suggested random co-assembly, whereas functional studies proposed 2:2 or 1:3 stoichiometries of KCNQ2:KCNQ3 [31-33]. The lack of direct structural information has thus hindered a mechanistic understanding of how subunit diversity gives rise to the distinctive gating and stability of the M-current.

Pharmacological targeting of KCNQ2/3 has proven clinically valuable yet challenging [34,35]. The first-generation opener retigabine (or ezogabine) enhanced M-currents and reduced seizures by stabilizing the open state but lacked subtype and stoichiometric selectivity, leading to adverse effects and market withdrawal [36-40]. The next-generation modulator XEN1101 shows improved potency, subtype selectivity, and tolerability [41], yet the structural basis of its selectivity remains unknown. Understanding how KCNQ2 and KCNQ3 assemble and interact is therefore critical for

elucidating the structural basis of neuronal excitability and for designing heteromer-selective modulators that maximize efficacy while minimizing side effects.

Over the past decade, cryo-electron microscopy (cryo-EM) has revolutionized our understanding of the KCNQ channel family [42]. Structures of cardiac KCNQ1 in complex with KCNE subunits revealed how auxiliary proteins modulate voltage sensing and gating [43-45], while high-resolution reconstructions of neuronal KCNQ2, KCNQ4, and KCNQ5 homomers provided detailed insights into gating, functional modulation, and drug binding [46-51]. The KCNQ channel family adopts the canonical tetrameric K_V channel structure in domain-swapped arrangement [42-53]. Each subunit contains six transmembrane segments (S1–S6) with S1–S4 forming the voltage-sensing domain (VSD) and the S5–S6 folding to the pore domain (PD). The C-terminal domain (CTD) contains three helices (HA, HB, and HC) that interact with the calcium-modulated protein calmodulin (CaM). During channel opening, HA/HB together with CaM undergo a ~180° rotation, transitioning the CTD from an "attached" (with VSD) to a "detached" conformation [43-51,53]. Within the transmembrane region, a conserved pocket at the interface of two adjacent PDs serves as the binding site for multiple activators [26,46-51,53]. These studies have established a mechanistic framework for KCNQ channel activation and pharmacology. However, all available structures to date represent homomeric assemblies, leaving the molecular architecture, subunit stoichiometry, and drug-binding pocket organization of the native KCNQ2/3 heteromer unresolved.

Here, we present the cryo-EM structures of the human KCNQ2/3 heteromer in both the apo state and in complex with the next-generation anticonvulsant XEN1101. Together with electrophysiological and pharmacological analyses, these structures reveal varying KCNQ2:KCNQ3 stoichiometries with a 1:3 assembly as the predominant form. This asymmetric assembly defines the molecular interfaces that shape gating and ligand recognition, and uncover how heteromerization creates a distinct pharmacological landscape. These findings resolve long-standing questions regarding KCNQ2/3 architecture and provide a structural foundation for the rational design of heteromer-selective modulators, paving the way toward safer and more effective therapies for epilepsy and other neurological disorders.

Results

Structure determination of the KCNQ2/3 heteromer channel

Functional M-channel requires the co-assembly of both KCNQ2 and KCNQ3 subunits [7,26-29]. To investigate the structural and functional properties of KCNQ2/3 heteromeric channels, we characterized their electrophysiological profiles in Chinese hamster ovary (CHO) cells. In line with previous findings [7,24,26-29], transfection of KCNQ2 alone yielded moderate, slowly activating potassium currents, while expression of KCNQ3 alone produced negligible currents (Fig. 1A). In contrast, co-expression of KCNQ2 and KCNQ3 at a 1:1 mass ratio resulted in a substantial increase in current amplitude, far exceeding that of KCNQ2 alone (Fig. 1A). This synergistic current increase indicates that heteromerization is essential for efficient channel trafficking and robust functional expression at the plasma membrane.

Given the high sequence identity (~70%) between the transmembrane regions of KCNQ2 and KCNQ3, unambiguous subunit assignment in cryo-EM maps was initially challenging. To isolate the heteromeric population, we co-expressed full-length human KCNQ2 and KCNQ3 with orthogonal affinity tags (Flag–KCNQ2 and Strep–KCNQ3), allowing tandem affinity purification to selectively enrich the KCNQ2/3 heteromer while excluding homomeric assemblies (Fig. S1A–C). The purified KCNQ2/3 complex yielded a cryo-EM reconstruction at an overall resolution of 3.6 Å (Fig. S1D, E). However, the lower local resolution in the transmembrane region and the high sequence similarity between KCNQ2 and KCNQ3 still precluded confident subunit assignment based solely on side-chain features.

To overcome this, we engineered a BRIL-fusion construct (KCNQ2–BRIL) by inserting apocytochrome b562RIL (BRIL) [54] into the S1-S2 linker of KCNQ2 (Fig. 1B), providing a distinct structural marker for unambiguous subunit identification. Crucially, the KCNQ2–BRIL/KCNQ3 channel produced robust current dynamics indistinguishable from wild-type KCNQ2/3 (Fig. 1C), validating that the fusion did not perturb channel function. Subsequent size-exclusion chromatography (SEC) yielded a single, symmetrical peak, and SDS-PAGE analysis of peak fractions confirmed co-elution of KCNQ2-BRIL and KCNQ3, verifying a stable heteromeric assembly (Fig. 1D, E).

From ~1,000,000 selected particles, we obtained multiple classes of KCNQ2/3 assemblies without imposing symmetry (Fig. S2A, B). Strikingly, 2D classification revealed four distinct

stoichiometries, corresponding to complexes containing 1, 2 (adjacent), 2 (diagonal), or 3 BRIL densities (Fig. 1F), consistent with variable KCNQ2 subunit(s) incorporation within the tetramer. Among these, the KCNQ2/3/3/3 (1:3) emerged as the predominant population, suggesting that this asymmetric stoichiometry represents the major physiological form of native M-channels.

To functionally test this hypothesis, we generated tandem-linked constructs enforcing defined subunit stoichiometries: KCNQ2/3/3/3 (1:3), KCNQ2/2/3/3 (2:2, adjacent), KCNQ2/3/2/3 (2:2, diagonal), and KCNQ2/2/2/3 (3:1). Whole-cell patch-clamp recordings demonstrated that all four tandem constructs generated robust currents (Fig. 1G). Importantly, the KCNQ2/3/3/3 tandem construct most closely recapitulated the biophysical properties of native KCNQ2/3 currents (Fig. 1G), providing functional evidence that the asymmetric 1:3 stoichiometry is the principal assembly state of the M-channel.

The KCNQ2/3 heteromer channel predominantly adopts a KCNQ2/3/3/3 stoichiometry

Refinement of the KCNQ2/3/3/3 class yielded a 3.0 Å map ($KCNQ2/3/3/3_{APO}$), in which the BRIL density enabled unambiguous subunit assignment and revealed an asymmetric 1:3 KCNQ2:KCNQ3 organization (Fig. 2A, S2C, D). A second reconstruction obtained in the presence of PIP_2 and the positive modulator XEN1101 ($KCNQ2/3/3/3_{PIP2}$, 3.2 Å) revealed an identical stoichiometry, with clear density for four PIP_2 and four XEN1101 molecules bound at equivalent inter-subunit interfaces (Fig. 2B, S3A-D).

To further validate this stoichiometry in a physiological context, we leveraged the known dramatic difference in tetraethylammonium (TEA) sensitivity between KCNQ2 and KCNQ3 [7,9,55,56]. Of note, we introduced the A315T mutation to address the absence of current in WT KCNQ3, thereby restoring normal current size in KCNQ3-A315T (pseudo-WT KCNQ3, or KCNQ3*) [57]. This different TEA sensitivity arises from a TEA binding residue tyrosine (Y284) following the signature sequence of the selectivity filter "TIGYG" in KCNQ2 ($IC_{50} = 0.18 \pm 0.04$ mM), versus a threonine substitution (T323) at the equivalent position in KCNQ3* ($IC_{50} > 100$ mM) (Fig. 2C, D). The resulting ~1000-fold difference provides a robust pharmacological fingerprint for determining the major stoichiometry of heteromeric KCNQ2/KCNQ3 channels. We therefore measured the TEA sensitivity of wild-type heteromeric KCNQ2/KCNQ3 channels alongside tandem-linked constructs of defined stoichiometries KCNQ2/3/3/3, KCNQ2/2/3/3, KCNQ2/3/2/3, and KCNQ2/2/2/3. Remarkably, the wild-type heteromer KCNQ2/KCNQ3 channels exhibited a TEA

sensitivity (IC_{50} = 31.4 ± 3.6 mM) that was significantly different from the 2:2 (KCNQ2/2/3/3, IC_{50} = 3.0 ± 0.5 mM, $p < 0.0001$, and KCNQ2/3/2/3, IC_{50} =2.5 ± 0.4 mM, $p < 0.0001$) and 3:1 (KCNQ2/2/2/3, IC_{50} = 0.7 ± 0.1 mM, $p < 0.0001$) constructs but indistinguishable from the 1:3 (KCNQ2/3/3/3, IC_{50} = 24.5 ± 5.1 mM, $p = 0.28$) tandem construct (Fig. 2E, F). This result provides independent functional evidence that native KCNQ2/3 heteromeric channels predominantly assemble with a 1:3 stoichiometry.

Overall architecture of the KCNQ2/3/3/3 channel

Our structural data reveal that while the KCNQ2/3 heteromer maintains the canonical domain-swapped architecture (Fig. 3A), key structural distinctions from the KCNQ2 homomer underlie its unique functional properties.

When viewed from the extracellular side, the VSDs of KCNQ2 and KCNQ3 subunits within the heteromer exhibit distinct counterclockwise rotations—approximately 8° and 12° respectively—resulting in an overall lateral expansion of the VSD (from 84.3 Å in KCNQ2 homomer to 88.5 Å in KCNQ2/3) (Fig. 3A). This rearrangement may subtly reshape the interdomain coupling between S4–S5 linkers and the pore domain, as well as the VSD-CTD interaction, thereby influencing the gating process and PIP2 modulation.

Notably, despite differences in their overall arrangement, the VSDs of all KCNQ2 and KCNQ3 subunits in both structures adopt a similar activated-state conformation, with conserved charge interactions comparable to the KCNQ2 homomer [26] (Fig. 3B). Specifically, E1 (E130 in KCNQ2, and E160 in KCNQ3) and F0 (F137 in KCNQ2, and F167 in KCNQ3) on the S2 helix engage with the gating charges R4 and H5 on the S4 helix, respectively (Fig. 3B). This similar VSD conformation between homomeric KCNQ2 and heteromeric KCNQ2/3 suggests that the observed functional differences arise primarily from the impact of heteromeric assembly on the energetics of conformational changes, rather than from a fundamental difference in the intrinsic state of the VSDs.

Pore analysis using HOLE revealed that the apo KCNQ2/3 channel adopts a closed conformation, with the inner gate residues S314 (KCNQ2) and S353 (KCNQ3) occluding the ion conduction pathway. In contrast, in the PIP_2-bound structure, the gate widens beyond ~3 Å, consistent with an open state (Fig. 3C–E). Detailed molecular dynamics (MD) simulations could be done to further confirm that the KCNQ2/3/3/3$_{PIP2}$ structure adopts an open conformation. Notably, the inherent

1:3 asymmetric stoichiometry imparts a structural asymmetry to the pore in both closed and open states (Fig. 3C), which may fine-tune the channel gating and pharmacology.

The most striking structural difference lies in the CTD. Prior studies have demonstrated that the opening of KCNQ2 homomer channel involves an approximately 180° rotation of its HA-HB helices together with CaM [26]. Interestingly, compared to the closed-state KCNQ2 homomer (PDB: 7CR3) [26], the HA-HB helices of the single KCNQ2 subunit and the three KCNQ3 subunits in the heteromer KCNQ2/3/3/3$_{APO}$ exhibit a ~30° pre-rotation in the apo state (Fig. 3F). During channel activation, all these HA-HB helices undergo a ~150° clockwise rotation to end up with a similar open conformation (Fig. 3F). This ~150° rotation is significantly smaller than the ~180° rotation observed in KCNQ2 homomers, indicating that the CTD in the heteromer is in a "pre-strained" state prior to activation. We propose that this pre-positioning effect, induced by the heteromerization with KCNQ3, lowers the activation energy barrier for the entire tetrameric channel, thereby providing a structural mechanism for the clearly leftward-shifted G-V curve observed for KCNQ2/3 heteromeric currents compared to KCNQ2 homomers (Fig. 3G).

Conserved and distinct intersubunit interactions in the heteromeric assembly

The high conformational similarity between KCNQ2 and KCNQ3 subunits enables the formation of a stable heterotetramer. Our structural analysis confirms that the heteromer retains key intersubunit interactions observed in homomers, such as a conserved hydrogen bond network near the selectivity filter formed by W309 and T313 in KCNQ3 and Y280 in KCNQ2, as well as an electrostatic interaction between R330 in KCNQ3 and D266 in the adjacent KCNQ2 subunit (Fig. S4A–F).

Despite this overall similarity, the heteromeric interfaces also exhibit unique characteristics. A prominent difference lies in the hydrophobic interactions at the interface between the S5 helix of one subunit and the VSD region of its neighbor. Notably, at the KCNQ3-KCNQ2 interface, I273 and F269 from KCNQ3 interact with L107, M208, and F104 from KCNQ2. In contrast, at the reciprocal KCNQ2-KCNQ3 interface, F104 in KCNQ2 is replaced by L134 in KCNQ3 (Fig. S4G, H). This substitution of a key residue may subtly alter the interfacial hydrophobic network, potentially serving as a structural basis for the "calibrated" voltage-dependent activation of the heteromer. Overall, while retaining canonical homomeric interactions, the KCNQ2/3 heteromer

incorporates specific interfacial differences, resulting in a uniquely assembled complex with optimized energetic properties.

The binding pocket of XEN1101 in the KCNQ2/3 heteromer channel

XEN1101 is a next-generation KCNQ2/3 channel opener with enhanced potassium efflux and suppresses neuronal hyperexcitability in epilepsy [41,58]. Compared with ezogabine, it exhibits superior subtype selectivity (KCNQ2/3 > KCNQ4) and pharmacokinetics, minimizing urological side effects [59]. Consistent with its design, we found 300 nM XEN1101 potently increased KCNQ2/3 currents and leftward shifted the voltage-dependence of activation curve (Fig. 4A, B). In the cryo-EM density, four XEN1101 molecules were clearly resolved at inter-subunit interfaces within the pore domain (Fig. 4C). Each ligand resides in a conserved hydrophobic pocket formed by two adjacent subunits. The compound establishes hydrogen bonds with W265, S342, and the backbone of L338 in KCNQ3 (corresponding to W236, S303, and L299 in KCNQ2) and π–π stacking with W265, complemented by extensive hydrophobic interactions with F269, P347, and I254 (Fig. 4D).

Mutational analysis corroborated these observations: 1) W236A(KCNQ2) and W265A(KCNQ3*) abolished XEN1101-induced activation (Fig. 4E–F); 2) F240A(KCNQ2), L299A(KCNQ2), I254A(KCNQ3*), F269A(KCNQ3*), L338A(KCNQ3*), S342A(KCNQ3*), F343A(KCNQ3*), and P347A(KCNQ3*) strongly reduced its efficacy (Fig. 4F); 3) V225A(KCNQ2), F304A(KCNQ2), and P308A(KCNQ2) showed non-detectable currents (Fig. S5), precluding further testing. These mutational results demonstrate the binding site of XEN1101 observed in KCNQ2/3/3/3$_{PIP2}$.

The fact that both KCNQ2(W236A) and KCNQ3*(W265A) mutations abolish XEN1101 sensitivity provides another pharmacological tool to functionally validate the 1:3 KCNQ2:KCNQ3 stoichiometry. We reasoned that the drug response of the heteromeric KCNQ2/3 channel would depend on its subunit composition. We thus co-expressed KCNQ2(W236A) with wild-type KCNQ3, and wild-type KCNQ2 with KCNQ3(W265A) (Fig. 4G). While the wild-type KCNQ2+KCNQ3 channel responded robustly to 100 nM and 300 nM XEN1101, the KCNQ2+KCNQ3(W265A) combination showed a significantly greater reduction in XEN1101 response than the KCNQ2(W236A)+KCNQ3 channel (Fig. 4G, H). This asymmetric effect also

indicates that KCNQ3 subunits dominate the heteromeric complex, providing another functional evidence consistent with the 1:3 stoichiometry.

Our structural data also highlighted the molecular basis for XEN1101's subtype selectivity among KCNQ channels [58,59]. Sequence alignment revealed that some key hydrophobic amino acids in the pocket are not conserved within the KCNQ family. For example, L272 in KCNQ2 (corresponding to L311 in KCNQ3) is T278 in KCNQ4. This substitution of amino acid residues may disrupt the hydrophobic cavity at the upper part of the binding pocket, thereby affecting the binding of XEN1101 in KCNQ4 (Fig. S6A–E).

PIP2 modulation in the KCNQ2/3 heteromer channel

Phosphatidylinositol 4,5-bisphosphate (PIP_2), a phosphoinositide lipid in the inner leaflet of the plasma membrane, serves as an essential cofactor for KCNQ channel activation [60-65]. In the KCNQ2/3/3/3$_{PIP2}$ structure, a well-defined density corresponding to PIP_2 was observed at the canonical interface between the VSD and PD. The inositol 1,4,5-trisphosphate head group engages a conserved set of basic residues from both subunits, R214, R87, R89, and K327 in KCNQ2, and K259 in KCNQ3, forming a conserved PIP_2-site configuration (Fig. 5A, B). This arrangement mirrors, yet subtly diverges from, the canonical PIP_2-binding motif previously described in homomeric KCNQ channels, suggesting a reorganization of the lipid–protein interface upon heteromerization.

To assess the functional relevance of this PIP_2-binding pocket, we systematically substituted the key basic residues with alanine. As predicted, most substitutions—including R89A, K214A, K230A, and K327A in KCNQ2, and R243A, K259A, and K366A in KCNQ3—produced right-shifted voltage-dependence of activation (Fig. 5D, E), consistent with weakened PIP_2 interaction and impaired stabilization of the open state [46,51,53]. Notably, R87A in KCNQ2 resulted in a moderate left-shift of the G–V curve, and R117A and R119A in KCNQ3 produced minimal gating changes, indicating a less direct contribution of these residues to PIP_2 modulation (Fig. 5D, E).

Further structural comparison between KCNQ2$_{PIP2}$ [46] and KCNQ2/3/3/3$_{PIP2}$ reveals that heteromerization enhances PIP_2 sensitivity by tightening the PIP_2-binding pocket (Fig. 5B, C). Although the PIP_2-binding pocket is largely conserved between two structures, we found that the pocket volume of the KCNQ2 homomeric structure is dramatically larger than those of the heteromer structure. This is evidenced by the R89-K366 distance, which is 11.2 Å in KCNQ2$_{PIP2}$,

while shortened to 8.8 Å in the KCNQ2/KCNQ3 subunit pocket (R119-K366) and to 7.3 Å in the KCNQ3/KCNQ3 subunit pocket (R119-K366) of the KCNQ2/3/3/3$_{PIP2}$ structure (Fig. 5B, C). This shortened distance likely strengthens the PIP_2-binding in M-channels. Furthermore, the asymmetric nature of the PIP2-binding may fine-tune the subunit-specific activation, diversifying PIP2-mediated modulation of M-channels in neuron cells.

Together, these findings establish a structural and functional basis for how PIP_2 modulates the KCNQ2/3 heteromer through cooperative, yet non-equivalent, subunit interactions (Fig. 5F). The dominance of KCNQ3 in the heteromeric interface likely underlies the unique gating behavior and pharmacological sensitivity that distinguish the neuronal M-current from its homomeric counterparts (Fig. 5F).

Discussion

The heterotetrameric KCNQ2/3 channel constitutes the molecular embodiment of the neuronal M-current, a cornerstone of neuronal excitability control. For decades, the fundamental architecture of this physiologically critical complex has remained a subject of debate. Our study resolves this long-standing question by revealing that the native KCNQ2/3 channel predominantly assembles in an asymmetric 1:3 (KCNQ2:KCNQ3) stoichiometry. This structural elucidation, combined with our functional data, allows us to move beyond mere description and propose a unified mechanism by which this specific stoichiometry gives rise to the defining properties of the M-current.

Our structural data provide a clear rationale for the prevalence of the 1:3 assembly. This configuration appears to be an optimal compromise, leveraging the distinct strengths of each subunit while mitigating their individual limitations. The single KCNQ2 subunit acts as a crucial linchpin, facilitating efficient tetramerization and membrane trafficking—a function that homomeric KCNQ3 fails to perform. Conversely, the trio of KCNQ3 subunits dominates the functional core of the channel. Structural analysis reveals that interfaces involving KCNQ2 exhibit distinct interaction networks, and we posit that incorporating additional KCNQ2 subunits would introduce less favorable interfacial energetics, making the 1:3 form the most stable and thus predominant assembly.

Our structural observation of the 1:3 KCNQ2/KCNQ3 assembly likely represents the stoichiometry of mature neuronal M-channels. This conclusion is supported by following evidence: 1) Developmental expression profile in the human brain (hippocampus, temporal lobe, cerebellum,

316 etc.) shows that KCNQ2 expression is high at birth and decreases over time, while KCNQ3
317 expression gradually increases [66]. Consistent with this, KCNQ2 deletion in mouse leads to
318 perinatal lethality, whereas KCNQ3 knockout mice are viable into adulthood [67-69]; 2) Data from
319 rat superior cervical ganglion neurons confirm this pattern: while the KCNQ2 level remains high
320 and stable, KCNQ3 expression increases during maturation [33]. Accordingly, TEA sensitivity
321 experiments show a corresponding shift in M-channel composition from KCNQ2-dominant in
322 young neurons to a greater KCNQ3 contribution in mature ones [9,33]. These complex spatiotemporal
323 expression patterns underscore the sophistication of M-channel assembly. Further structural
324 studies in native neurons are essential for advancing precision medicine therapies.
325 A cardinal feature of the M-current is its activation at subthreshold membrane potentials [70], a
326 property directly explained by our structures. We find that the asymmetric assembly creates a
327 uniquely reconfigured voltage-sensing apparatus. The heteromeric VSD is laterally expanded, and
328 the C-terminal domain (CTD) of the solitary KCNQ2 subunit is pre-positioned in a ~30° rotated
329 state in the closed conformation. We hypothesize that this pre-activation of the KCNQ2 CTD
330 serves as a molecular trigger, effectively lowering the allosteric energy barrier for channel opening.
331 This mechanism, where the pre-strained KCNQ2 subunit primes the entire tetramer for activation,
332 allows the channel to open in response to smaller depolarizations, thereby "calibrating" the voltage
333 dependence to perfectly suit its role in stabilizing the resting potential.
334 Beyond gating, the 1:3 stoichiometry fundamentally defines the channel's pharmacological
335 identity. The clinical need for subtype-selective KCNQ modulators is underscored by the history
336 of retigabine. Our structural and mutagenesis data demonstrate that XEN1101 selectivity is an
337 emergent property of the heteromer. With three of its four identical drug-binding pockets primarily
338 constituted by KCNQ3, the channel's pharmacological profile is intrinsically set to be "KCNQ3-
339 like". This KCNQ3-dominated chemical environment is optimally complementary to XEN1101,
340 while divergent residues in other homologs like KCNQ4 create suboptimal binding sites. Thus,
341 the heteromer does not merely combine subunits; it creates a novel pharmacological entity that is
342 selectively targeted by next-generation therapeutics.
343 In conclusion, we propose that neurons utilize the 1:3 KCNQ2:KCNQ3 stoichiometry not as a
344 simple compromise, but as a sophisticated structural strategy to create de novo a potassium channel
345 with optimized properties. This asymmetric assembly integrates the trafficking proficiency of
346 KCNQ2 with the gating and pharmacological landscape shaped by KCNQ3, all while introducing

unique functional advantages through reconfigured domain coupling and pre-activation. Our work thus provides a comprehensive structural framework that deciphers the molecular logic of the M-current. It settles fundamental debates and opens a new chapter for the rational design of precision medicines targeting KCNQ2/3-related epilepsies and other disorders of neuronal hyperexcitability.

Acknowledgments

We would like to thank the Cryo-EM center of Shuimu BioSciences for our Cryo-EM work and their help of Cryo-EM data collection. This work was Supported by School of Basic Medical Sciences, Nanchang University.

Funding

This work was supported by the National Natural Science Foundation of China (grant # 32271260 to J.Z.), the CAS "Light of West China" Program (xbzg-zdsys-202005 to J.Z.), the Shenzhen Science and Technology Program (grant no. JCYJ20220818103017036 and KJZD20240903102205008 to J.Z.) and the Jiangxi Province Natural Science Foundation (grant no. 20224ACB206046 to J.Z.). P.H. was supported by the National Natural Science Foundation of China (32171221), the Joint Funding of the Macau Science and Technology Development Fund and the Ministry of Science and Technology of China (0006/2021/AMJ), and the Macau Science and Technology Development Fund (0074/2022/A2, 0098/2023/RIA2, 002/2023/ALC, and 006/2023/SKL). B.H. acknowledges support from the Science and Technology Research Project of Jiangxi Provincial Department of Education (GJJ2201447) and the Jiangxi Provincial Natural Science Foundation (20252BAC240521).

Author Contributions

P.H. and J.Z. conceived the project, designed the research and supervised the study. X.C., S.W., D.J., H.Z., B.H., W.N., Z.Z., C.X., L.Z., Y.Z., P.H., and J.Z. performed experiments. X.C., S.W., D.J., H.Z., B.H., T.C., W.N., Z.Z., C.X., L.Z., Y.Z., P.H., and J.Z. analyzed data. B.Y., O.L., J.D., B.X., P.H., and J.Z. provided key intellectual expertise and methodologies. X.C., S.W., D.J., H.Z., B.H., P.H., and J.Z. wrote the manuscript with input from all authors.

Competing interests

The authors declare no competing interests.

Data availability

377 The atomic coordinates and cryo-EM density maps for KCNQ2/3$_{apo}$ and KCNQ2/3-XEN1101-
378 PIP_2 have been deposited in the Protein Data Bank and Electron Microscopy Data Bank,
379 respectively. The accession codes for KCNQ2/3$_{apo}$ in this paper are 9X5J and EMDB-66589. The
380 accession codes for KCNQ2/3-XEN1101-PIP_2 in this paper are 9X65 and EMDB-66607. Source
381 data are provided with this paper.
382
383

Methods

Constructs and mutagenesis

The full-length human KCNQ2 construct, containing a C-terminal triple FLAG tag (DYKDHDGDYKDHDIDYKDDDDK), and the full-length human KCNQ3 construct, featuring an N-terminal Twin-Strep-Tag II (WSHPQFEKGGGSGGGSGGSAWSHPQFEK), were obtained by PCR and then subcloned into the pEGBacMam expression vector using EcoRI and NotI restriction sites. Overlap extension and high-fidelity PCR were used to generate point mutations in the KCNQ2 or KCNQ3 channels. Additionally, four multimeric fusion proteins were constructed using the Hieff Clone® Universal One Step Cloning Kit (YEASEN): KCNQ2/3/3/3(1:3), KCNQ2/2/3/3(2:2, adjacent), KCNQ2/3/2/3(2:2, diagonal), and KCNQ2/2/2/3(3:1). Each full-length subunit was amplified by PCR to obtain the corresponding DNA fragments, which included a flexible linker between subunits to ensure proper folding and interaction [43]. These four fragments were then mixed with the pEGBacMam expression vector and subjected to one-step cloning according to the manufacturer's instructions. Briefly, the linearized vector and the four subunit fragments were combined with the reaction buffer and enzyme mixture, incubated at 50°C for 30 min, and transformed into competent *E.coli* cells. All mutations and constructs were confirmed by DNA sequencing.

Protein expression and purification

Overlap extension and high-fidelity PCR were used, which was confirmed by DNA sequencing. The truncated KCNQ2 construct (residues 64–674), containing an N-terminal triple FLAG tag (DYKDHDGDYKDHDIDYKDDDDK), and the truncated KCNQ3 construct (residues 93 to 649), featuring an N-terminal Twin-Strep-Tag II (WSHPQFEKGGGSGGGSGGSAWSHPQFEK), were used for cloning the KCNQ2/3 heteromers construct into the pEGBacMam expression vector with a C-terminal Maltose Binding Protein. To enable unambiguous particle alignment, we aimed to introduce features that would increase particle size and provide an asymmetric shape, facilitating the differentiation of distinct subunits in KCNQ2/3 heteromers for 3D reconstruction. We therefore introduced the BRIL domain (cytochrome b562 RIL) [71,72] fused in place of extracellular loop 1 of KCNQ2. The human CaM gene was cloned into the pEGBacMam expression vector without any tags. Recombinant human KCNQ2/3 heteromer expressed in mammalian HEK293 F cells using transient transfection. When the cell concentration reached 2.0–3.0 × 10^6 cells per milliliter, the

cells were cotransfected with three types of plasmids corresponding to KCNQ2, KCNQ3, and CaM at a mass ratio of 5:5:1. For a 1-liter HEK293 F cell culture, approximately 1 mg of the aforementioned mixed plasmids was first pre-blended with linear polyethyleneimines (PEIs, from MKbio) in 50 ml of fresh medium, and this plasmid-PEI mixture was allowed to stand for 15 to 30 minutes. Subsequently, the mixture was added to the cell culture, which was then incubated for 15 minutes. Following 24 hours of incubation at 37°C, 10 mM sodium butyrate was introduced and maintained at 30°C. The cells were collected after 48 hours, and kept at -80°C for future use. Cell pellets were resuspended in hypotonic buffer (20 mM Tris-HCl pH 8.0, 20 mM KCl, 0.5 mM $MgCl_2$, 2 mM DTT) with Selleck's protease inhibitor, gently agitated for 40 min. Crude membranes were collected by ultracentrifugation at 105,400×g for 45 min, then resuspended and solubilized in buffer (20 mM Tris-HCl pH 8.0, 150 mM KCl, 2 mM DTT, 0.5% LMNG:CHS 10:1) at 4°C for 2-2.5 h. After centrifugation, the supernatant was incubated with GenScript Anti-DYKDDDDK G1 Affinity Resin at 4°C for 2 h. The resin was washed with buffers containing different detergents (sequentially 0.1% LMNG+0.01% CHS+0.1% GDN, 0.1% GDN, 0.05% GDN) for 10 column volumes each. The proteins were then eluted with wash buffer plus 300 to 400 μg/mL FLAG peptide. The eluent from the anti-FLAG column was subsequently applied to the Strep-Tactin resin (IBA) and incubated at 4°C for 1 hour. The resin was thoroughly washed with the same buffer, then the target was eluted with the buffer plus 5 mM D-Desthiobiotin (Macklin). The protein eluent was purified via GE's Superose 6 Column equilibrated with 20 mM Tris-HCl pH 8.0, 150 mM KCl, 2 mM DTT, 0.03% GDN. Peak fractions were pooled, concentrated to 4-5 mg/mL with 100-kDa concentrator for cryo-EM. For KCNQ2/3 bound to XEN1101, the purified protein was incubated with 0.2 mM XEN1101 and 1 mM Echelon's diC8-PIP_2.

Cryo-EM sample preparation and data acquisition

To prepare the grids, 2.5–3.0 μL of the concentrated protein complex was applied to glow-discharged holey carbon grids (Quantifoil Au R1.2/1.3, 300 mesh) at 4°C under 100% humidity. The grids were blotted for 3.5 seconds and plunge-frozen in liquid ethane using a Vitrobot Mark IV (FEI). Micrographs were captured with a Titan Krios microscope (FEI) running at 300 kV. A detailed summary of the data collection is provided in Supplementary Table S1.

Cryo-EM data processing

Images of all datasets were imported into cryoSPARC v4.1.1 [73,74]. Cryo-EM movies were motion-corrected using MotionCor2 [75]. Contrast transfer functions (CTFs) were calculated using the patch

CTF estimation module. The initial particles were picked by Blob picker. The picked particles were extracted and classified with 2D classification and the best 2D classes were selected as the template. Then the particles were picked by template picker and extracted with a box size of 400 pixels (binned by 2) and classified with 2D classification. The sorted particles were subjected to heterogenous refinement using initial models generated by ab-initio reconstruction. The final particle sets were re-extracted with original box size and further applied for final nonuniform refinement and local refinement.

Model building and refinement for cryo-EM structures

All maps were sharpened using the B-factor automatically calculated in CryoSPARC. For the KCNQ2/3 heteromer, an AlphaFold model of the human KCNQ3 from AlphaFold Protein Structure Database [76] (UniProt accession code: O43525) and the structure of the human KCNQ2 apo state (Protein Data Bank (PDB) code: 7CR3) [26] were used to generate initial templates for model building. For the KCNQ2/3-XEN1101-PIP_2, our model of the KCNQ2/3 heteromer in this study (PDB code: 9X5J). All models were manually adjusted in Coot 0.9.8.1 [77,78]. The models were further refined by several rounds of real-space refinement in Phenix and were validated using MolProbity tool in Phenix [79]. The final refinement statistics are provided in Table 1. All structure figures were prepared in UCSF ChimeraX [80].

Cell culture and transfection

Chinese hamster ovary (CHO) cells were grown in F-12 (Gibco) supplemented with 10% fetal bovine serum (FBS). To transiently express the channel for electrophysiological studies, cells were seeded into 24-well plates and then transfected with 800 ng of the cDNA using the Lipofectamine 2000 reagent (Invitrogen) according to the manufacturer's guideline. A GFP cDNA (500 ng) was co-transfected to aid identification of transfected cells by fluorescence microscopy. For electrophysiological recordings, the cells were plated onto glass coverslips coated with poly-D-lysine and cultured in wells of sterile 24-well tissue culture plates in a humidified incubator at 37 °C, 5% CO_2, until use.

Electrophysiological recording

Standard whole-cell voltage-clamp recording was conducted at room temperature with EPC10 amplifier with the Patchmaster software (HEKA, Lambrecht, Germany). Pipettes were pulled from borosilicate glass capillaries (World Precision Instruments) with tip resistances of 3–7 MΩ when filled with the intracellular solution. The intracellular solution contained (in mM): 145 KCl, 5

NaCl, 2.5 $MgCl_2$, 5 EGTA, 10 HEPES (pH 7.3 adjusted by KOH); and the bath solution contained (in mM): 145 NaCl, 5 KCl, 1.8 $CaCl_2$, 1 $MgCl_2$, 10 HEPES, and 11 glucose (pH 7.3 adjusted by NaOH). The data were filtered at 2 kHz and digitized using Clampfit 10.3 software. Series resistance compensation was used and set to 80%.

Electrophysiology Data analysis

Data were analyzed with Clampfit (Axon Instruments), Sigmaplot (SPSS), and Prism (Graphpad). G–V curves were fitted with Boltzmann equations in the form of $1/(1+ \exp(-z*F*(V-V1/2)/RT))$, where V is the voltage, z is the equivalent valence, $V_{1/2}$ is the half-maximal voltage, F is the Faraday constant, R is the gas constant, and T is the absolute temperature. $V_{1/2}$ were estimated by fitting G–V relations of each channel with a single Boltzmann equation.

Statistical analysis

Averaged data were presented as mean ± standard error of mean (SEM) with n specifying the number of independent experiments. Statistical analyses (t-test, paired t-test, one-way ANOVA and post-hoc mean comparison Tukey test or Dunnett test) were performed with Sigmaplot (SPSS) and R software (4.1.2 version, multcomp package). Statistical significance was set as "*" $P < 0.05$, "**" $P < 0.01$, and "***" $P < 0.001$.

References

1 Chen, Y. H. *et al.* KCNQ1 gain-of-function mutation in familial atrial fibrillation. *Science* **299**, 251-254, doi:10.1126/science.1077771 (2003).

2 Schroeder, B. C., Kubisch, C., Stein, V. & Jentsch, T. J. Moderate loss of function of cyclic-AMP-modulated KCNQ2/KCNQ3 K+ channels causes epilepsy. *Nature* **396**, 687-690, doi:10.1038/25367 (1998).

3 Kubisch, C. *et al.* KCNQ4, a novel potassium channel expressed in sensory outer hair cells, is mutated in dominant deafness. *Cell* **96**, 437-446, doi:10.1016/s0092-8674(00)80556-5 (1999).

4 Robbins, J. KCNQ potassium channels: physiology, pathophysiology, and pharmacology. *Pharmacol Ther* **90**, 1-19, doi:10.1016/s0163-7258(01)00116-4 (2001).

5 Fidzinski, P. *et al.* KCNQ5 K(+) channels control hippocampal synaptic inhibition and fast network oscillations. *Nat Commun* **6**, 6254, doi:10.1038/ncomms7254 (2015).

6 Huang, H. & Trussell, L. O. KCNQ5 channels control resting properties and release probability of a synapse. *Nat Neurosci* **14**, 840-847, doi:10.1038/nn.2830 (2011).

7 Wang, H. S. *et al.* KCNQ2 and KCNQ3 potassium channel subunits: molecular correlates of the M-channel. *Science* **282**, 1890-1893, doi:10.1126/science.282.5395.1890 (1998).

8 Cooper, E. C. Made for "anchorin": Kv7.2/7.3 (KCNQ2/KCNQ3) channels and the modulation of neuronal excitability in vertebrate axons. *Semin Cell Dev Biol* **22**, 185-192, doi:10.1016/j.semcdb.2010.10.001 (2011).

9 Shapiro, M. S. *et al.* Reconstitution of muscarinic modulation of the KCNQ2/KCNQ3 K(+) channels that underlie the neuronal M current. *J Neurosci* **20**, 1710-1721, doi:10.1523/jneurosci.20-05-01710.2000 (2000).

10 Jentsch, T. J. Neuronal KCNQ potassium channels: physiology and role in disease. *Nat Rev Neurosci* **1**, 21-30, doi:10.1038/35036198 (2000).

11 Kato, M. *et al.* Clinical spectrum of early onset epileptic encephalopathies caused by KCNQ2 mutation. *Epilepsia* **54**, 1282-1287, doi:10.1111/epi.12200 (2013).

12 Weckhuysen, S. *et al.* KCNQ2 encephalopathy: emerging phenotype of a neonatal epileptic encephalopathy. *Ann Neurol* **71**, 15-25, doi:10.1002/ana.22644 (2012).

13 Miceli, F. *et al.* A novel KCNQ3 mutation in familial epilepsy with focal seizures and intellectual disability. *Epilepsia* **56**, e15-20, doi:10.1111/epi.12887 (2015).

14 Singh, N. A. *et al.* A novel potassium channel gene, KCNQ2, is mutated in an inherited epilepsy of newborns. *Nat Genet* **18**, 25-29, doi:10.1038/ng0198-25 (1998).

15 Charlier, C. *et al.* A pore mutation in a novel KQT-like potassium channel gene in an idiopathic epilepsy family. *Nat Genet* **18**, 53-55, doi:10.1038/ng0198-53 (1998).

16 Passmore, G. M. *et al.* KCNQ/M currents in sensory neurons: significance for pain therapy. *J Neurosci* **23**, 7227-7236, doi:10.1523/jneurosci.23-18-07227.2003 (2003).

17 Zheng, Q. *et al.* Suppression of KCNQ/M (Kv7) potassium channels in dorsal root ganglion neurons contributes to the development of bone cancer pain in a rat model. *Pain* **154**, 434-448, doi:10.1016/j.pain.2012.12.005 (2013).

18 Kalappa, B. I. *et al.* Potent KCNQ2/3-specific channel activator suppresses in vivo epileptic activity and prevents the development of tinnitus. *J Neurosci* **35**, 8829-8842, doi:10.1523/jneurosci.5176-14.2015 (2015).

19 Sands, T. T. *et al.* Autism and developmental disability caused by KCNQ3 gain-of-function variants. *Ann Neurol* **86**, 181-192, doi:10.1002/ana.25522 (2019).

20 Wang, J. *et al.* Activation of Neuronal Voltage-Gated Potassium Kv7/KCNQ/M-Current by a Novel Channel Opener SCR2682 for Alleviation of Chronic Pain. *J Pharmacol Exp Ther* **377**, 20-28, doi:10.1124/jpet.120.000357 (2021).

21 Zheng, Y. *et al.* Activation of peripheral KCNQ channels relieves gout pain. *Pain* **156**, 1025-1035, doi:10.1097/j.pain.0000000000000122 (2015).

22 Miceli, F., Soldovieri, M. V., Weckhuysen, S., Cooper, E. & Taglialatela, M. in *GeneReviews(®)* (eds M. P. Adam *et al.*) (University of Washington, Seattle
Copyright © 1993-2025, University of Washington, Seattle. GeneReviews is a registered trademark of the University of Washington, Seattle. All rights reserved., 1993).
23 Carotenuto, L. *et al.* The fast-dissociating D(2) antagonist antipsychotic JNJ-37822681 is a neuronal Kv7 channel opener: Potential repurposing for epilepsy treatment. *Br J Pharmacol* **182**, 5574-5595, doi:10.1111/bph.70119 (2025).
24 Hinojo-Perez, A. *et al.* The conductance of KCNQ2 and its pathogenic variants is determined by individual subunit gating. *Sci Adv* **11**, eadr7012, doi:10.1126/sciadv.adr7012 (2025).
25 Brown, D. A. & Adams, P. R. Muscarinic suppression of a novel voltage-sensitive K+ current in a vertebrate neurone. *Nature* **283**, 673-676, doi:10.1038/283673a0 (1980).
26 Li, X. *et al.* Molecular basis for ligand activation of the human KCNQ2 channel. *Cell Res* **31**, 52-61, doi:10.1038/s41422-020-00410-8 (2021).
27 Gómez-Posada, J. C. *et al.* A pore residue of the KCNQ3 potassium M-channel subunit controls surface expression. *J Neurosci* **30**, 9316-9323, doi:10.1523/jneurosci.0851-10.2010 (2010).
28 Choveau, F. S., De la Rosa, V., Bierbower, S. M., Hernandez, C. C. & Shapiro, M. S. Phosphatidylinositol 4,5-bisphosphate (PIP(2)) regulates KCNQ3 K(+) channels by interacting with four cytoplasmic channel domains. *J Biol Chem* **293**, 19411-19428, doi:10.1074/jbc.RA118.005401 (2018).
29 Suh, B. C. & Hille, B. Recovery from muscarinic modulation of M current channels requires phosphatidylinositol 4,5-bisphosphate synthesis. *Neuron* **35**, 507-520, doi:10.1016/s0896-6273(02)00790-0 (2002).
30 Yang, N. D. *et al.* Electro-mechanical coupling of KCNQ channels is a target of epilepsy-associated mutations and retigabine. *Sci Adv* **8**, eabo3625, doi:10.1126/sciadv.abo3625 (2022).
31 Springer, K., Varghese, N. & Tzingounis, A. V. Flexible Stoichiometry: Implications for KCNQ2- and KCNQ3-Associated Neurodevelopmental Disorders. *Dev Neurosci* **43**, 191-200, doi:10.1159/000515495 (2021).
32 Stewart, A. P. *et al.* The Kv7.2/Kv7.3 heterotetramer assembles with a random subunit arrangement. *J Biol Chem* **287**, 11870-11877, doi:10.1074/jbc.M111.336511 (2012).
33 Hadley, J. K. *et al.* Stoichiometry of expressed KCNQ2/KCNQ3 potassium channels and subunit composition of native ganglionic M channels deduced from block by tetraethylammonium. *J Neurosci* **23**, 5012-5019, doi:10.1523/jneurosci.23-12-05012.2003 (2003).
34 Costi, S. *et al.* Impact of the KCNQ2/3 Channel Opener Ezogabine on Reward Circuit Activity and Clinical Symptoms in Depression: Results From a Randomized Controlled Trial. *Am J Psychiatry* **178**, 437-446, doi:10.1176/appi.ajp.2020.20050653 (2021).
35 Costi, S., Han, M. H. & Murrough, J. W. The Potential of KCNQ Potassium Channel Openers as Novel Antidepressants. *CNS Drugs* **36**, 207-216, doi:10.1007/s40263-021-00885-y (2022).
36 Porter, R. J., Nohria, V. & Rundfeldt, C. Retigabine. *Neurotherapeutics* **4**, 149-154, doi:10.1016/j.nurt.2006.11.012 (2007).
37 Deeks, E. D. Retigabine (ezogabine): in partial-onset seizures in adults with epilepsy. *CNS Drugs* **25**, 887-900, doi:10.2165/11205950-000000000-00000 (2011).
38 Stafstrom, C. E., Grippon, S. & Kirkpatrick, P. Ezogabine (retigabine). *Nat Rev Drug Discov* **10**, 729-730, doi:10.1038/nrd3561 (2011).
39 Gunthorpe, M. J., Large, C. H. & Sankar, R. The mechanism of action of retigabine (ezogabine), a first-in-class K+ channel opener for the treatment of epilepsy. *Epilepsia* **53**, 412-424, doi:10.1111/j.1528-1167.2011.03365.x (2012).
40 Garin Shkolnik, T. *et al.* Blue-gray mucocutaneous discoloration: a new adverse effect of ezogabine. *JAMA Dermatol* **150**, 984-989, doi:10.1001/jamadermatol.2013.8895 (2014).
41 French, J. A. *et al.* Efficacy and Safety of XEN1101, a Novel Potassium Channel Opener, in Adults With Focal Epilepsy: A Phase 2b Randomized Clinical Trial. *JAMA Neurol* **80**, 1145-1154, doi:10.1001/jamaneurol.2023.3542 (2023).

42 Sun, J. & MacKinnon, R. Cryo-EM Structure of a KCNQ1/CaM Complex Reveals Insights into Congenital Long QT Syndrome. *Cell* **169**, 1042-1050.e1049, doi:10.1016/j.cell.2017.05.019 (2017).

43 Zhong, L. *et al.* Secondary structure transitions and dual PIP2 binding define cardiac KCNQ1-KCNE1 channel gating. *Cell Res*, doi:10.1038/s41422-025-01182-9 (2025).

44 Sun, J. & MacKinnon, R. Structural Basis of Human KCNQ1 Modulation and Gating. *Cell* **180**, 340-347.e349, doi:10.1016/j.cell.2019.12.003 (2020).

45 Cui, C. *et al.* Mechanisms of KCNQ1 gating modulation by KCNE1/3 for cell-specific function. *Cell Res*, doi:10.1038/s41422-025-01152-1 (2025).

46 Ma, D. *et al.* Ligand activation mechanisms of human KCNQ2 channel. *Nat Commun* **14**, 6632, doi:10.1038/s41467-023-42416-x (2023).

47 Zheng, Y. *et al.* Structural insights into the lipid and ligand regulation of a human neuronal KCNQ channel. *Neuron* **110**, 237-247.e234, doi:10.1016/j.neuron.2021.10.029 (2022).

48 Yang, Z. *et al.* Phosphatidylinositol 4,5-bisphosphate activation mechanism of human KCNQ5. *Proc Natl Acad Sci U S A* **122**, e2416738122, doi:10.1073/pnas.2416738122 (2025).

49 Zhang, S. *et al.* A small-molecule activation mechanism that directly opens the KCNQ2 channel. *Nat Chem Biol* **20**, 847-856, doi:10.1038/s41589-023-01515-y (2024).

50 Li, J. *et al.* Small molecule inhibits KCNQ channels with a non-blocking mechanism. *Nat Chem Biol* **21**, 1100-1109, doi:10.1038/s41589-024-01834-8 (2025).

51 Li, T. *et al.* Structural Basis for the Modulation of Human KCNQ4 by Small-Molecule Drugs. *Mol Cell* **81**, 25-37.e24, doi:10.1016/j.molcel.2020.10.037 (2021).

52 Long, S. B., Campbell, E. B. & Mackinnon, R. Crystal structure of a mammalian voltage-dependent Shaker family K+ channel. *Science* **309**, 897-903, doi:10.1126/science.1116269 (2005).

53 Ma, D. *et al.* Structural mechanisms for the activation of human cardiac KCNQ1 channel by electro-mechanical coupling enhancers. *Proc Natl Acad Sci U S A* **119**, e2207067119, doi:10.1073/pnas.2207067119 (2022).

54 Chun, E. *et al.* Fusion partner toolchest for the stabilization and crystallization of G protein-coupled receptors. *Structure* **20**, 967-976, doi:10.1016/j.str.2012.04.010 (2012).

55 Hadley, J. K. *et al.* Differential tetraethylammonium sensitivity of KCNQ1-4 potassium channels. *Br J Pharmacol* **129**, 413-415, doi:10.1038/sj.bjp.0703086 (2000).

56 Etxeberria, A., Santana-Castro, I., Regalado, M. P., Aivar, P. & Villarroel, A. Three mechanisms underlie KCNQ2/3 heteromeric potassium M-channel potentiation. *J Neurosci* **24**, 9146-9152, doi:10.1523/jneurosci.3194-04.2004 (2004).

57 Zaika, O., Hernandez, C. C., Bal, M., Tolstykh, G. P. & Shapiro, M. S. Determinants within the turret and pore-loop domains of KCNQ3 K+ channels governing functional activity. *Biophys J* **95**, 5121-5137, doi:10.1529/biophysj.108.137604 (2008).

58 Bialer, M. *et al.* Progress report on new antiepileptic drugs: A summary of the Fourteenth Eilat Conference on New Antiepileptic Drugs and Devices (EILAT XIV). I. Drugs in preclinical and early clinical development. *Epilepsia* **59**, 1811-1841, doi:10.1111/epi.14557 (2018).

59 Bialer, M. *et al.* Progress report on new antiepileptic drugs: A summary of the Fifteenth Eilat Conference on New Antiepileptic Drugs and Devices (EILAT XV). I. Drugs in preclinical and early clinical development. *Epilepsia* **61**, 2340-2364, doi:10.1111/epi.16725 (2020).

60 Zhang, H. *et al.* PIP(2) activates KCNQ channels, and its hydrolysis underlies receptor-mediated inhibition of M currents. *Neuron* **37**, 963-975, doi:10.1016/s0896-6273(03)00125-9 (2003).

61 Zaydman, M. A. *et al.* Kv7.1 ion channels require a lipid to couple voltage sensing to pore opening. *Proc Natl Acad Sci U S A* **110**, 13180-13185, doi:10.1073/pnas.1305167110 (2013).

62 Kim, R. Y., Pless, S. A. & Kurata, H. T. PIP2 mediates functional coupling and pharmacology of neuronal KCNQ channels. *Proc Natl Acad Sci U S A* **114**, E9702-e9711, doi:10.1073/pnas.1705802114 (2017).

63 Falkenburger, B. H., Jensen, J. B. & Hille, B. Kinetics of PIP2 metabolism and KCNQ2/3 channel regulation studied with a voltage-sensitive phosphatase in living cells. *J Gen Physiol* **135**, 99-114, doi:10.1085/jgp.200910345 (2010).

64 Zhang, Q. *et al.* Dynamic PIP2 interactions with voltage sensor elements contribute to KCNQ2 channel gating. *Proc Natl Acad Sci U S A* **110**, 20093-20098, doi:10.1073/pnas.1312483110 (2013).
65 Zhong, L. *et al.* Targeting the I(Ks) Channel PKA Phosphorylation Axis to Restore Its Function in High-Risk LQT1 Variants. *Circ Res* **135**, 722-738, doi:10.1161/circresaha.124.325009 (2024).
66 Kanaumi, T. *et al.* Developmental changes in KCNQ2 and KCNQ3 expression in human brain: possible contribution to the age-dependent etiology of benign familial neonatal convulsions. *Brain Dev* **30**, 362-369, doi:10.1016/j.braindev.2007.11.003 (2008).
67 Watanabe, H. *et al.* Disruption of the epilepsy KCNQ2 gene results in neural hyperexcitability. *J Neurochem* **75**, 28-33, doi:10.1046/j.1471-4159.2000.0750028.x (2000).
68 Tzingounis, A. V. & Nicoll, R. A. Contribution of KCNQ2 and KCNQ3 to the medium and slow afterhyperpolarization currents. *Proc Natl Acad Sci U S A* **105**, 19974-19979, doi:10.1073/pnas.0810535105 (2008).
69 Soh, H., Pant, R., LoTurco, J. J. & Tzingounis, A. V. Conditional deletions of epilepsy-associated KCNQ2 and KCNQ3 channels from cerebral cortex cause differential effects on neuronal excitability. *J Neurosci* **34**, 5311-5321, doi:10.1523/jneurosci.3919-13.2014 (2014).
70 Marrion, N. V. Control of M-current. *Annu Rev Physiol* **59**, 483-504, doi:10.1146/annurev.physiol.59.1.483 (1997).
71 Mukherjee, S. *et al.* Synthetic antibodies against BRIL as universal fiducial marks for single-particle cryoEM structure determination of membrane proteins. *Nat Commun* **11**, 1598, doi:10.1038/s41467-020-15363-0 (2020).
72 Liu, W. *et al.* Structural basis for allosteric regulation of GPCRs by sodium ions. *Science* **337**, 232-236, doi:10.1126/science.1219218 (2012).
73 Punjani, A., Rubinstein, J. L., Fleet, D. J. & Brubaker, M. A. cryoSPARC: algorithms for rapid unsupervised cryo-EM structure determination. *Nat Methods* **14**, 290-296, doi:10.1038/nmeth.4169 (2017).
74 Punjani, A., Zhang, H. & Fleet, D. J. Non-uniform refinement: adaptive regularization improves single-particle cryo-EM reconstruction. *Nat Methods* **17**, 1214-1221, doi:10.1038/s41592-020-00990-8 (2020).
75 Zheng, S. Q. *et al.* MotionCor2: anisotropic correction of beam-induced motion for improved cryo-electron microscopy. *Nat Methods* **14**, 331-332, doi:10.1038/nmeth.4193 (2017).
76 Abramson, J. *et al.* Accurate structure prediction of biomolecular interactions with AlphaFold 3. *Nature* **630**, 493-500, doi:10.1038/s41586-024-07487-w (2024).
77 Emsley, P., Lohkamp, B., Scott, W. G. & Cowtan, K. Features and development of Coot. *Acta Crystallogr D Biol Crystallogr* **66**, 486-501, doi:10.1107/s0907444910007493 (2010).
78 Emsley, P. & Cowtan, K. Coot: model-building tools for molecular graphics. *Acta Crystallogr D Biol Crystallogr* **60**, 2126-2132, doi:10.1107/s0907444904019158 (2004).
79 Adams, P. D. *et al.* PHENIX: a comprehensive Python-based system for macromolecular structure solution. *Acta Crystallogr D Biol Crystallogr* **66**, 213-221, doi:10.1107/s0907444909052925 (2010).
80 Goddard, T. D. *et al.* UCSF ChimeraX: Meeting modern challenges in visualization and analysis. *Protein Sci* **27**, 14-25, doi:10.1002/pro.3235 (2018).

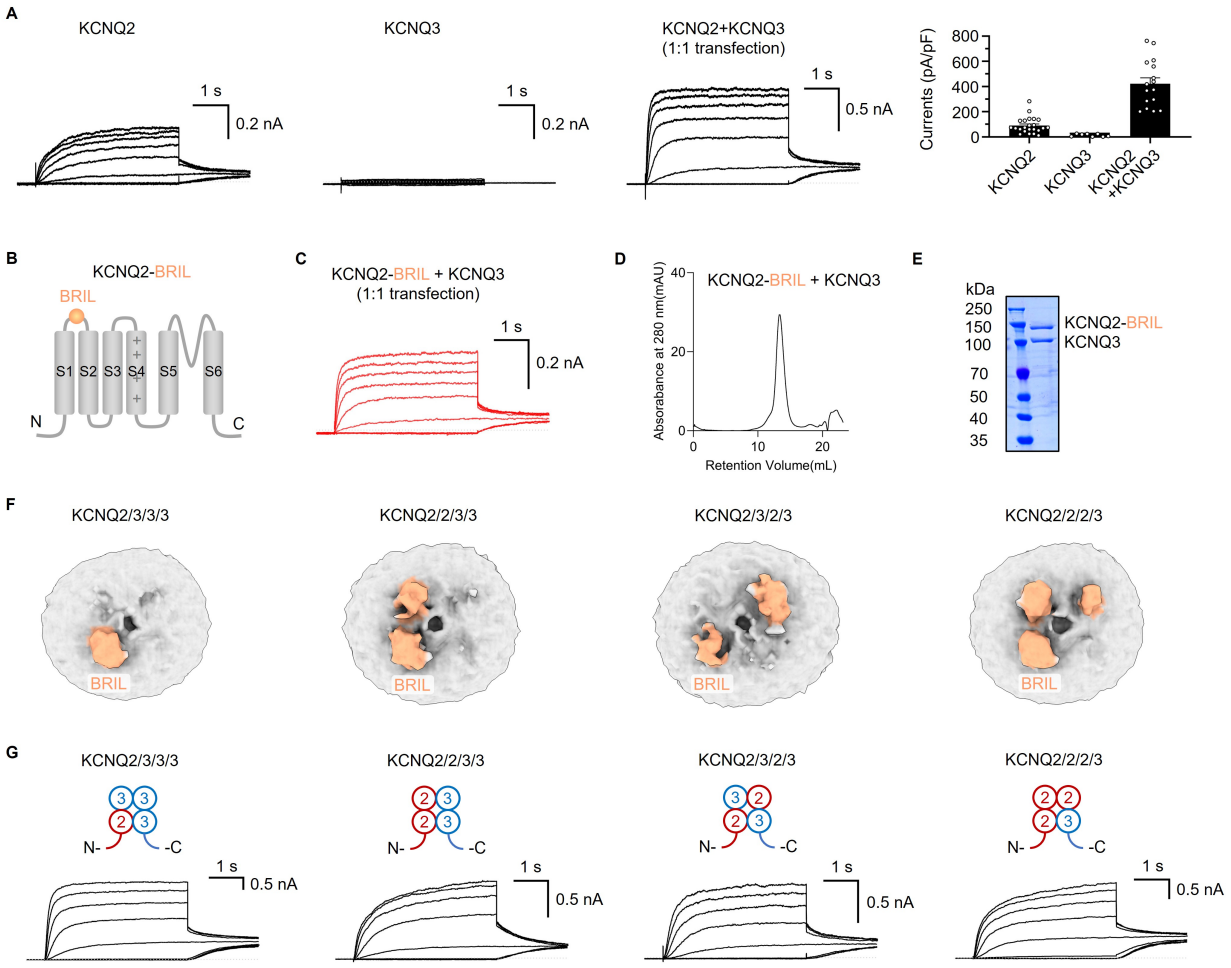

Figure 1. Functional M channels contain KCNQ2 and KCNQ3 in different stoichiometry. (A) Representative activation currents and current densities of KCNQ2, KCNQ3 and KCNQ2 + KCNQ3 (1:1 mass ratio transfection). Current densities at +40 mV were 90.2 ± 13.2 pA/pF for KCNQ2(n = 23), 13.7 ± 3.9 pA/pF for KCNQ3 (n = 8), and 422.1 ± 46.9 pA/pF for KCNQ2+KCNQ3 (n = 16). **(B)** Schematic diagram of KCNQ2 cloning construct. **(C)** Representative activation currents of KCNQ2-BRIL + KCNQ3(1:1 mass ratio transfection). **(D)** KCNQ2/3 heteromer size exclusion chromatography (SEC) trace obtained using an FPLC equipped with Superose 6 Increase 10/300 column. **(E)** Corresponding SDS-PAGE Coomassie-stained gel of the collected sample off the column. **(F)** Density maps of KCNQ2/3 with different subunit composition ratios. The BRIL density is shown in orange. **(G)** Representative activation currents of KCNQ2/3/3/3, KCNQ2/2/3/3, KCNQ2/3/2/3 and KCNQ2/2/2/3.

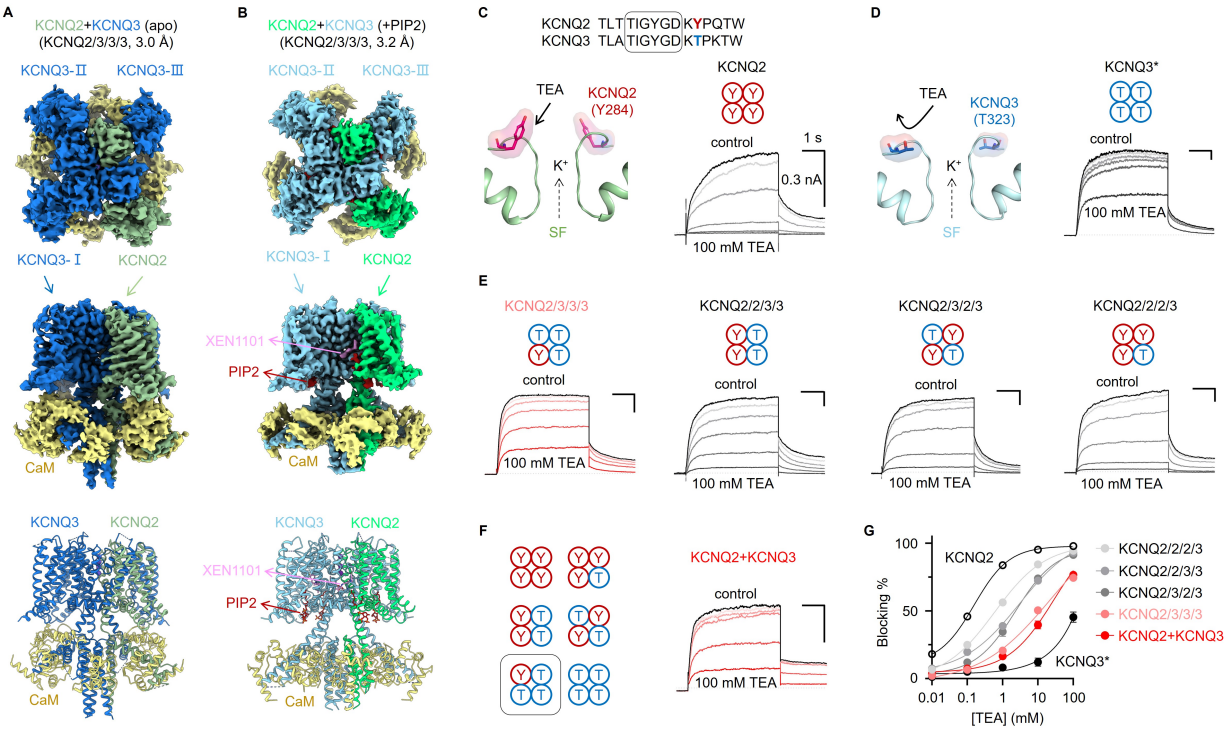

Figure 2. The primary KCNQ2/3 heteromer channel adopts a KCNQ2/3/3/3 stoichiometry. **(A)** Top and side views of KCNQ2/3 density maps in the apo condition and side views of structure models. Color code: KCNQ2 (dark green), KCNQ3 (deep blue), and CaM (yellow). **(B)** Top and side views of KCNQ2/3-XEN1101-PIP_2 density maps in the open condition and side views of structure models. Color code: KCNQ2 (light green), KCNQ3 (light blue), and CaM (yellow). **(C-D)** Sequence alignment to show the principle of different TEA sensitivity between KCNQ2 and KCNQ3. The TEA binding residue Y284 in KCNQ2 is substituted with T323 in KCNQ3. Representative currents of KCNQ2 and KCNQ3* (KCNQ3-A315T), before and after adding TEA (with concentrations 0.01 mM, 0.1 mM, 1 mM, 10 mM, and 100 mM). **(E)** Representative activation currents KCNQ2/3/3/3, KCNQ2/2/3/3, KCNQ2/3/2/3, and KCNQ2/2/2/3 before and after adding TEA (from 0.01 mM to 100 mM). **(F)** Representative activation currents of KCNQ2 + KCNQ3 (1:1 mass ratio), before and after adding TEA (from 0.01 mM to 100 mM), and a cartoon scheme to show that KCNQ2/3/3/3 (harboring Y/T/T/T at TEA binding sites) most closely recapitulated the TEA block of native KCNQ2/3 channels. **(G)** TEA blocking dose response of KCNQ2 + KCNQ3 (red) and KCNQ2/3/3/3 (pink). Dose response of KCNQ2, KCNQ3 and other heteromers are also shown. IC_{50} = 31.4 ± 3.6 mM for KCNQ2 + KCNQ3 (n = 11); IC_{50} = 24.5 ± 5.1 mM for KCNQ2/3/3/3 (n = 11); IC_{50} = 0.2 ± 0.1 mM for KCNQ2 (n = 9); IC_{50} = 0.7 ± 0.1 mM

718 for KCNQ2/2/2/3 ($n = 9$); $IC_{50} = 3.0 \pm 0.5$ mM for KCNQ2/2/3/3 ($n = 8$); $IC_{50} = 2.5 \pm 0.4$ mM for

719 KCNQ2/3/2/3 ($n = 11$); $IC_{50} > 100$ mM for KCNQ3* ($n = 5$).

720

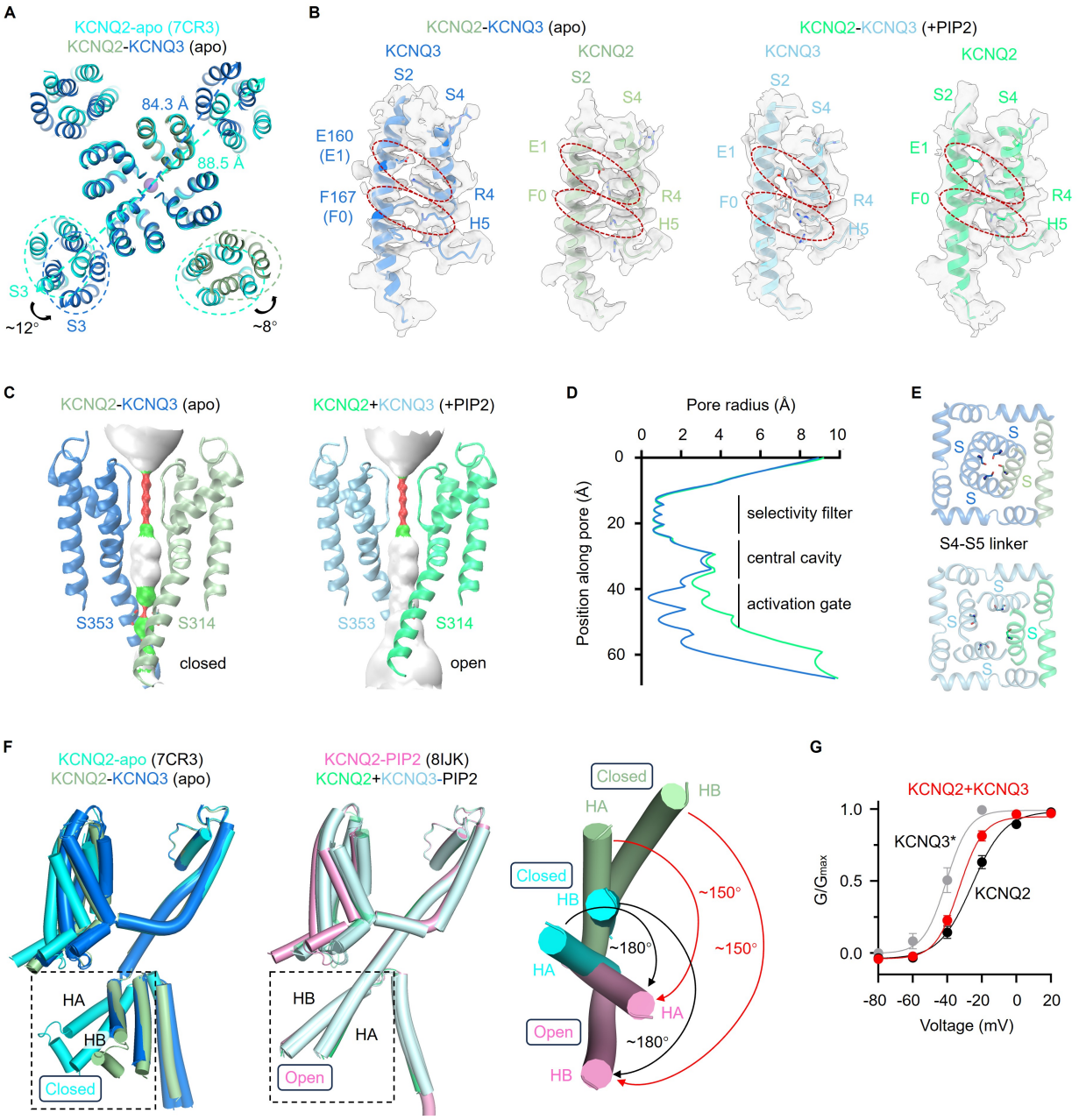

721

722 **Figure 3. Heteromerization-induced structural changes on KCNQ2/3/3/3. (A)** Horizontal
723 expansion of the voltage-sensing domain (VSD) of KCNQ2/3 and KCNQ2. Structures were
724 aligned to the filter. **(B)** Structural comparison of VSD states between KCNQ2-KCNQ3$_{apo}$ and
725 KCNQ2-KCNQ3$_{PIP2}$. Only S2 and S4 were shown for clarity. **(C)** Example pore radius analysis of
726 KCNQ2-KCNQ3$_{apo}$ and KCNQ2-KCNQ3$_{PIP2}$ with front and back subunits excluded for clarity. **(D)**
727 Pore radius analysis of KCNQ2-KCNQ3$_{apo}$ (blue) and KCNQ2-KCNQ3$_{PIP2}$ (green). **(E)** Structural
728 comparison of the activation gate between KCNQ2-KCNQ3$_{apo}$ and KCNQ2-KCNQ3$_{PIP2}$. **(F)** Left,
729 structural comparison to show that the CTD of KCNQ2-KCNQ3$_{apo}$ is in a "pre-positioned" state,

730 compared to KCNQ2apo (cyan, 7CR3)[26]. Middle, structural comparison to show that the CTD of
731 KCNQ2-KCNQ3$_{PIP2}$ is in a similar state to KCNQ2$_{PIP2}$ (pink, 8IJK)[49]. Right, structural comparison
732 to show that, due to the "pre-positioned" state of CTD, the HA-HB helices of KCNQ2-KCNQ3
733 heteromeric channel undergo a significantly smaller (~150° vs ~180° in KCNQ2 homomer)
734 rotation during channel opening. **(G)** G–V relations of KCNQ2 + KCNQ3 (1:1 mass ratio
735 transfection), KCNQ3* (gray) and KCNQ2 (black). $V_{1/2}$ = -25.7 ± 1.9 mV for KCNQ2 (n = 10);
736 $V_{1/2}$ = -33.1 ± 1.9 mV for KCNQ2 (n = 15); and $V_{1/2}$ = -40.7 ± 2.2 mV for KCNQ3* (n = 7).
737

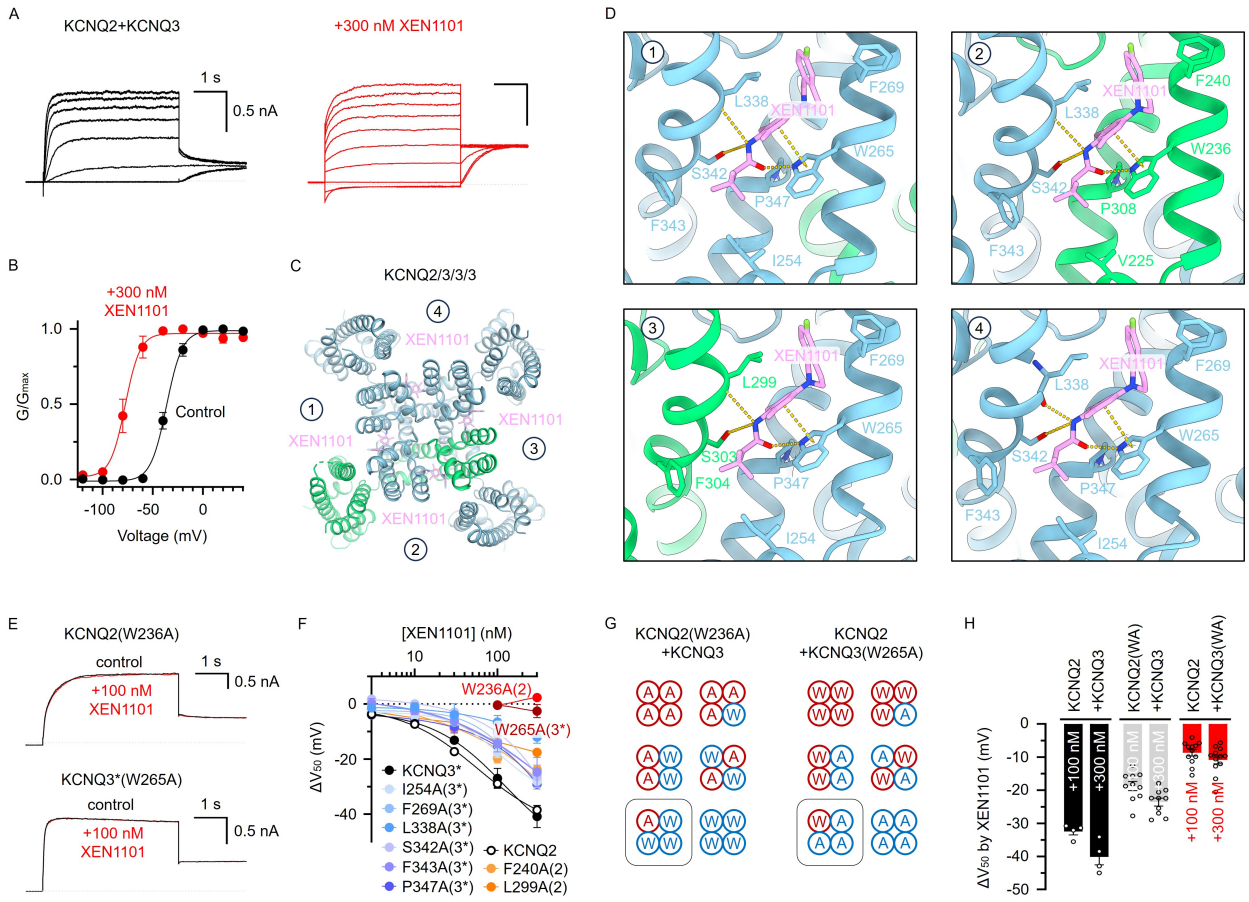

Figure 4. XEN1101 activation of KCNQ2/3/3/3. (A) Representative activation currents of KCNQ2+KCNQ3 (1:1 mass ratio transfection), before and after adding 300 nM XEN1101. **(B)** G–V relation of KCNQ2 + KCNQ3, before and after adding 300 nM XEN1101. **(C)** Top view of XEN1101 binding site in KCNQ2/3-XEN1101-PIP_2. **(D)** Local magnified image of the XEN1101 binding site in KCNQ2/3-XEN1101-PIP_2. **(E)** Representative activation currents of KCNQ2(W236A) and KCNQ3*(W265A) before and after adding 100 nM XEN1101. These channel currents were recorded at 40 mV. **(F)** Dose response of the voltage changes in the $V_{1/2}$ ($\Delta V_{1/2}$) caused by XEN1101 in KCNQ2, KCNQ3* and XEN1101 binding sites. $EC_{50} = 57.4 \pm 7.1$ nM for KCNQ2 ($n = 9$); $EC_{50} = 92.0 \pm 7.6$ nM for KCNQ3* ($n = 6$); $EC_{50} = 204.2 \pm 7.5$ nM for I254A (KCNQ3*) ($n = 8$); $EC_{50} = 232.9 \pm 20.7$ nM for F269A (KCNQ3*) ($n = 4$); $EC_{50} = 234.6 \pm 12.0$ nM for S342A (KCNQ3*) ($n = 5$); $EC_{50} = 207.5 \pm 21.7$ nM for S343A (KCNQ3*) ($n = 5$); $EC_{50} = 255.2 \pm 14.9$ nM for S347A (KCNQ3*) ($n = 4$); $EC_{50} = 136.7 \pm 2.2$ nM for F240A (KCNQ2) ($n = 9$). **(G)** Cartoon schemes to show the KCNQ2 and KCNQ3 assembly of KCNQ2(W236A)+KCNQ3 (harboring A/W/W/W at XEN1101 binding site) and

KCNQ2+KCNQ3(W265A) (harboring W/A/A/A at XEN1101 binding site). The KCNQ2/3/3/3 assemblies in both schemes were highlighted in black squares. **(H)** Comparison of the voltage changes in the $V_{1/2}$ ($\Delta V_{1/2}$) caused by 100 nM and 300 nM XEN1101 in KCNQ2 + KCNQ3 (1:1 mass ratio transfection, black), KCNQ2(W236A) + KCNQ3 (1:1 mass ratio transfection, gray) and KCNQ2 + KCNQ3(W265A) (1:1 mass ratio transfection, red).

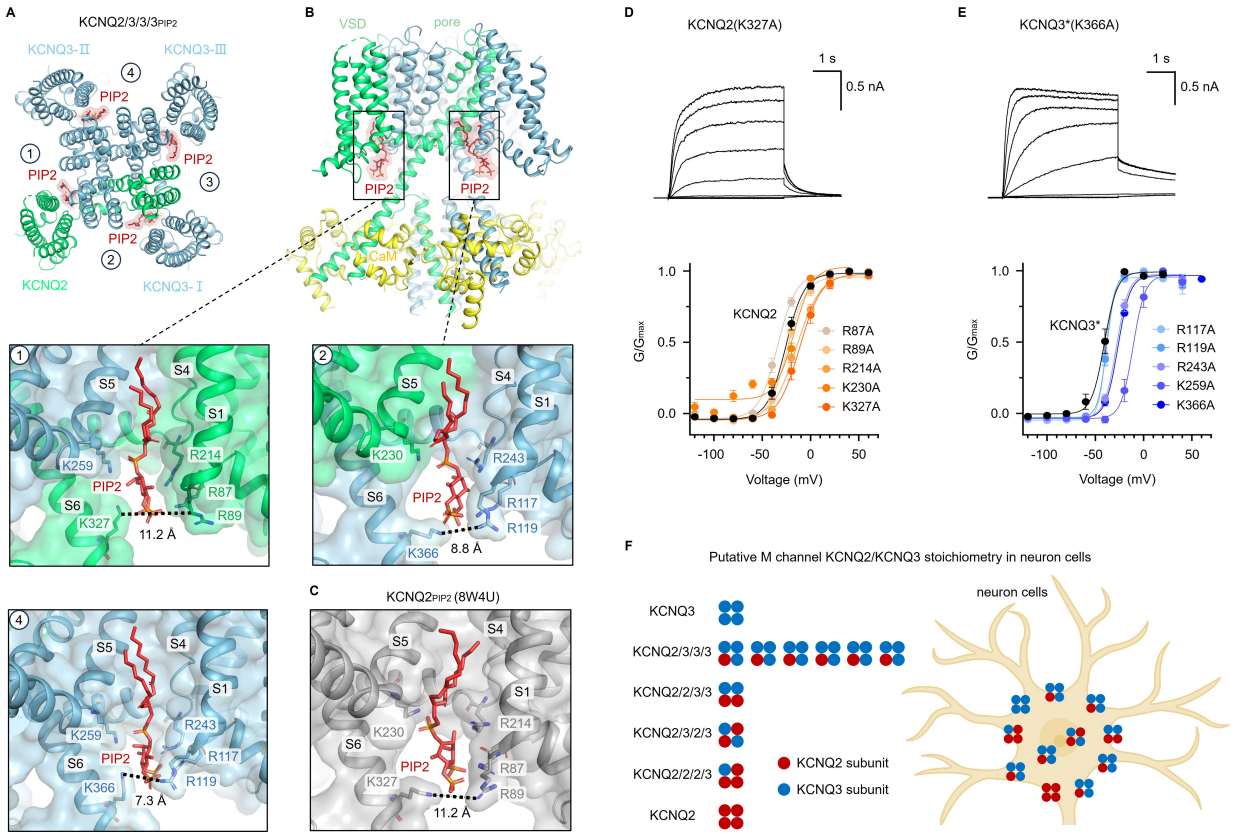

Figure 5. PIP2 modulation of KCNQ2/3/3/3. (A) Top view of PIP_2 binding site in KCNQ2/3-XEN1101-PIP_2. **(B)** Local magnified image of the PIP_2 binding site in KCNQ2/3-XEN1101-PIP_2. **(C)** Local magnified image of the PIP_2 binding site in KCNQ2 (8W4U)[46]. **(D)** KCNQ2 (K327A) currents and G–V relations of alanine mutagenesis scanning of PIP2 binding residues in KCNQ2: $V_{1/2}$ = -25.7 ± 1.9 mV for KCNQ2 (n = 10); $V_{1/2}$ = -34.2 ± 2.0 mV for R87A (n = 10); $V_{1/2}$ = -24.0 ± 1.9 mV for R89A (n = 12); $V_{1/2}$ = -14.5 ± 3.0 mV for K214A (n = 5); $V_{1/2}$ = -17.3 ± 4.2 mV for R230A (n = 4); $V_{1/2}$ = -11.1 ± 2.9 mV for K327A (n = 5); **(E)** KCNQ3 (K366A) currents and G–V relations of alanine mutagenesis scanning of PIP2 binding residues in KCNQ3*: $V_{1/2}$ = -40.7 ± 2.2 mV for KCNQ3* (n = 7); $V_{1/2}$ = -39.0 ± 1.3 mV for R117A (n = 5); $V_{1/2}$ = -38.2 ± 1.6 mV for R119A (n = 5); $V_{1/2}$ = -28.2 ± 1.4 mV for R243A (n = 5); $V_{1/2}$ = -11.1 ± 2.9 mV for R259A (n = 5); $V_{1/2}$ = -26.7 ± 1.4 mV for K366A (n = 5). **(F)** Putative M channel KCNQ2/KCNQ3 stoichiometry in neuron cells

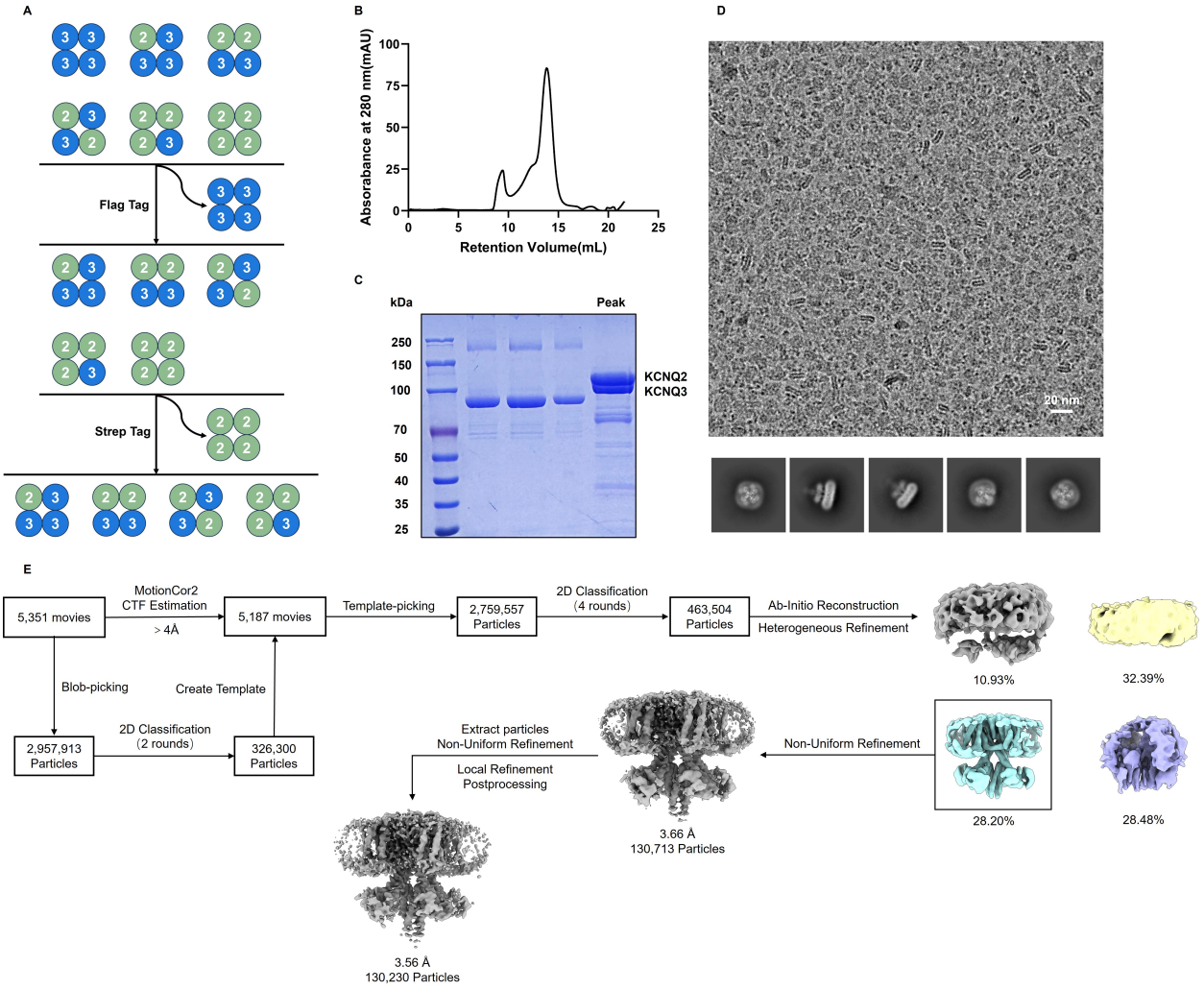

Figure S1. Purification and data processing of full-length KCNQ2/3 heteromers. (A) Schematic diagram of tandem affinity purification steps: first purify the protein with Flag tag, and then purify the protein with Strep tag. Flag-KCNQ2 (green); Strep-KCNQ3 (blue). **(B)** KCNQ2/3 heteromer size exclusion chromatography (SEC) trace obtained using an FPLC equipped with Superose 6 Increase 10/300 column. **(C)** Corresponding SDS-PAGE Coomassie-stained gel of the collected sample off the column. **(D)** Cryo-EM raw images of KCNQ2/3 heteromer and typical particles of KCNQ2/3 heteromer. **(E)** Summary of the image processing procedures of KCNQ2/3 heteromer.

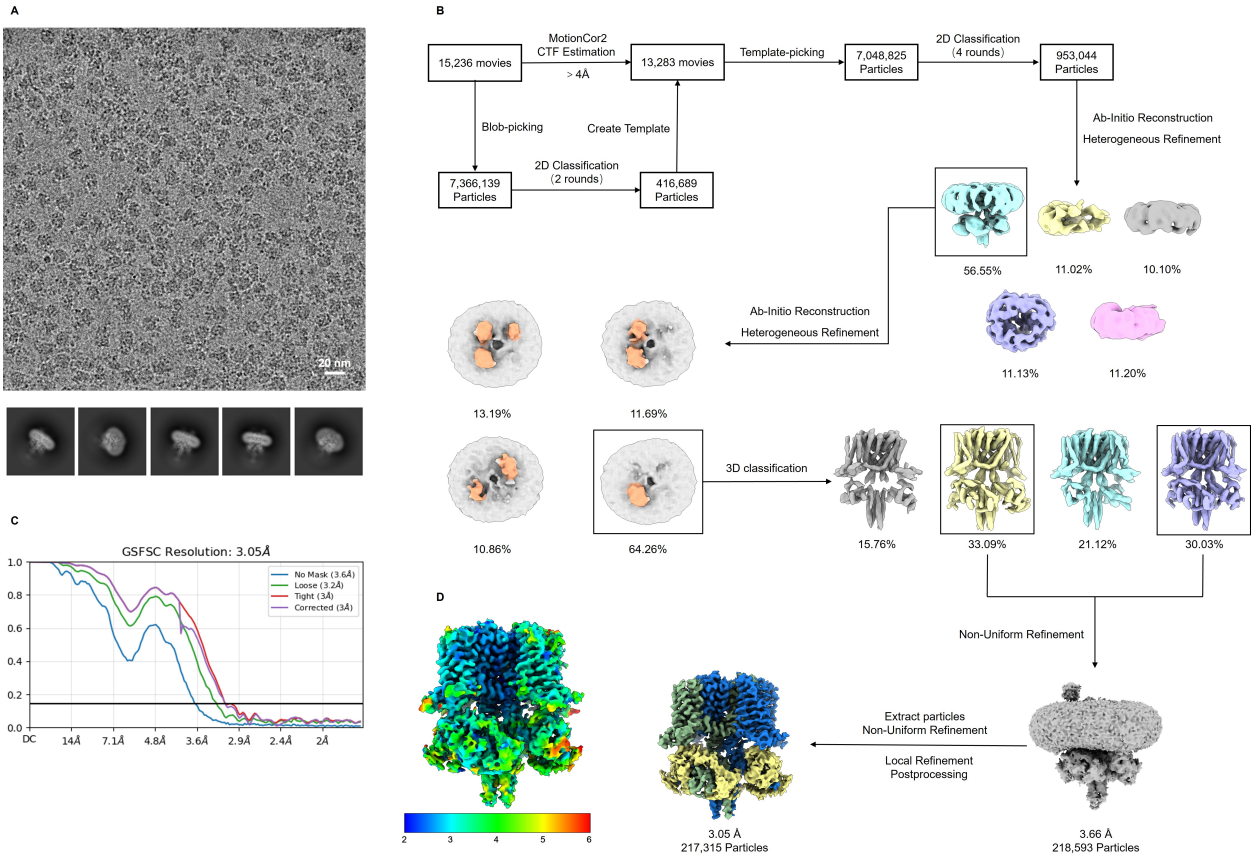

Figure S2. Cryo-EM and data processing of KCNQ2/3/3/3$_{APO}$. (A) Cryo-EM raw images of KCNQ2/3/3/3 and typical particles of KCNQ2/3/3/3. **(B)** Summary of the image processing procedures of KCNQ2/3/3/3. **(C)** Fourier shell correlation (FSC) curves of the final reconstruction from cryoSPARC for KCNQ2/3/3/3. **(D)** Local resolution estimation map using cryoSPARC for KCNQ2/3/3/3.

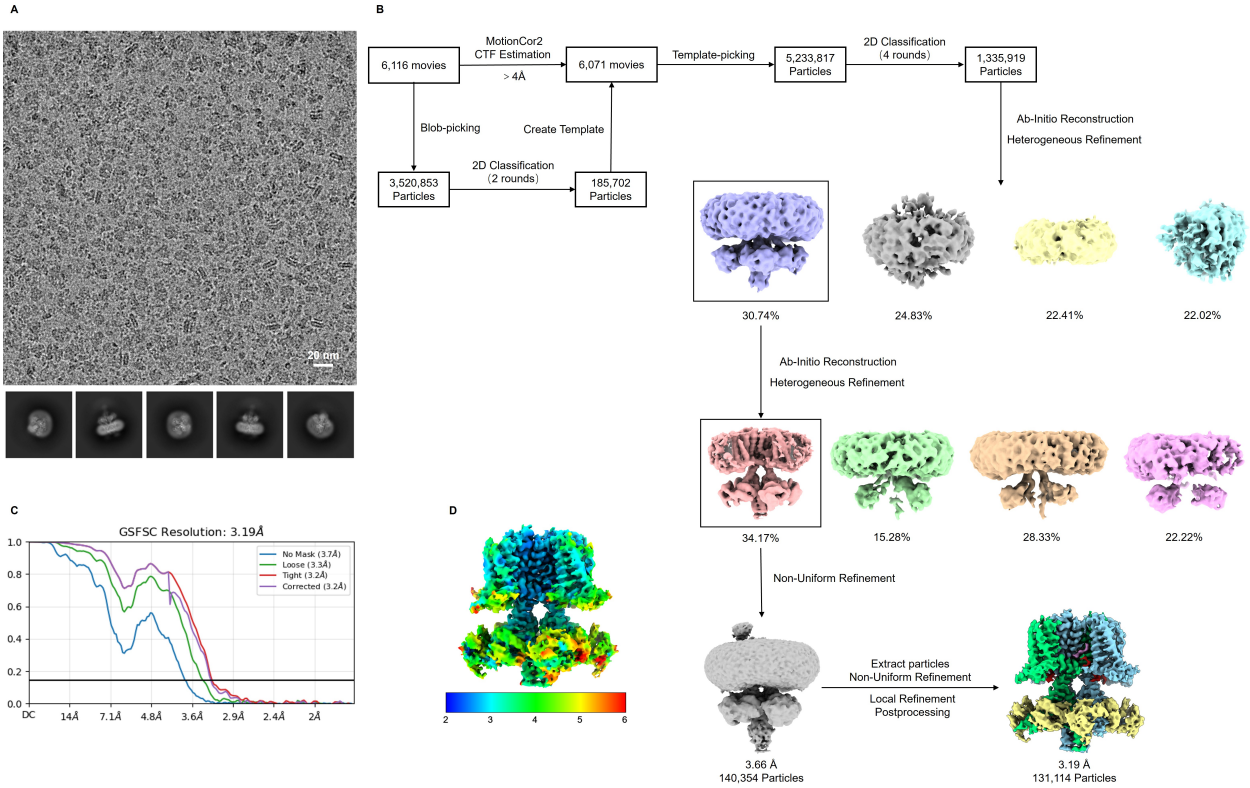

Figure S3. Cryo-EM and data processing of KCNQ2/3-XEN1101-PIP$_2$. (A) Cryo-EM raw images of KCNQ2/3-XEN1101-PIP$_2$ and typical particles of KCNQ2/3-XEN1101-PIP$_2$. **(B)** Summary of the image processing procedures of KCNQ2/3-XEN1101-PIP$_2$. **(C)** Fourier shell correlation (FSC) curves of the final reconstruction from cryoSPARC for KCNQ2/3-XEN1101-PIP$_2$. **(D)** Local resolution estimation map using cryoSPARC for KCNQ2/3-XEN1101-PIP$_2$.

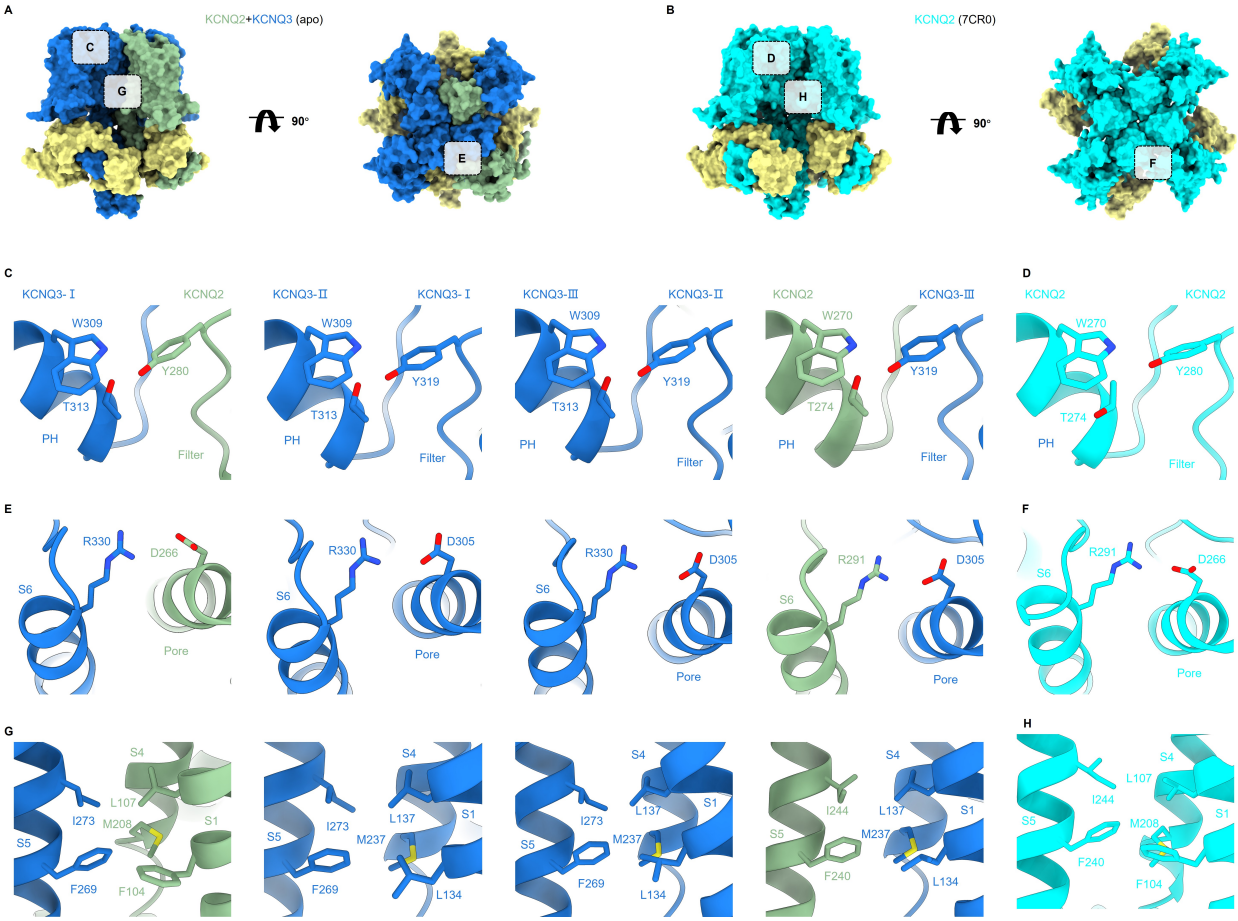

Figure S4. Intersubunit interactions. (A) Atomic surface representations of the KCNQ2/3/3/3 viewed from the side (left) and top (right). **(B)** Atomic surface representations of the KCNQ2 homomer viewed from the side (left) and top (right). Dotted boxes indicate intersubunit junctions expanded in C-H. Close-up views of the pore of the KCNQ2/3/3/3 **(C)** and KCNQ2 homomer **(D)**. Close-up views of S6 and pore of the KCNQ2/3/3/3 **(E)** and KCNQ2 homomer **(F)**. Close-up views of the VSD of the KCNQ2/3/3/3 **(G)** and KCNQ2 homomer **(H)**.

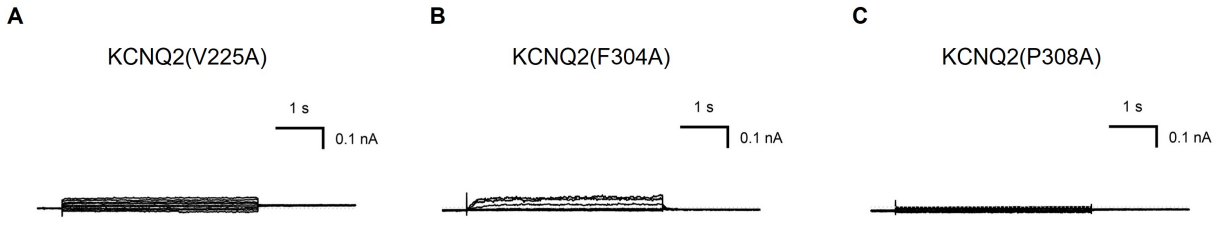

Figure S5. Non-detectable currents mutation in KCNQ2. (A) Representative activation currents of V225A (KCNQ2). **(B)** Representative activation currents of F304A (KCNQ2). **(C)** Representative activation currents of P308A (KCNQ2).

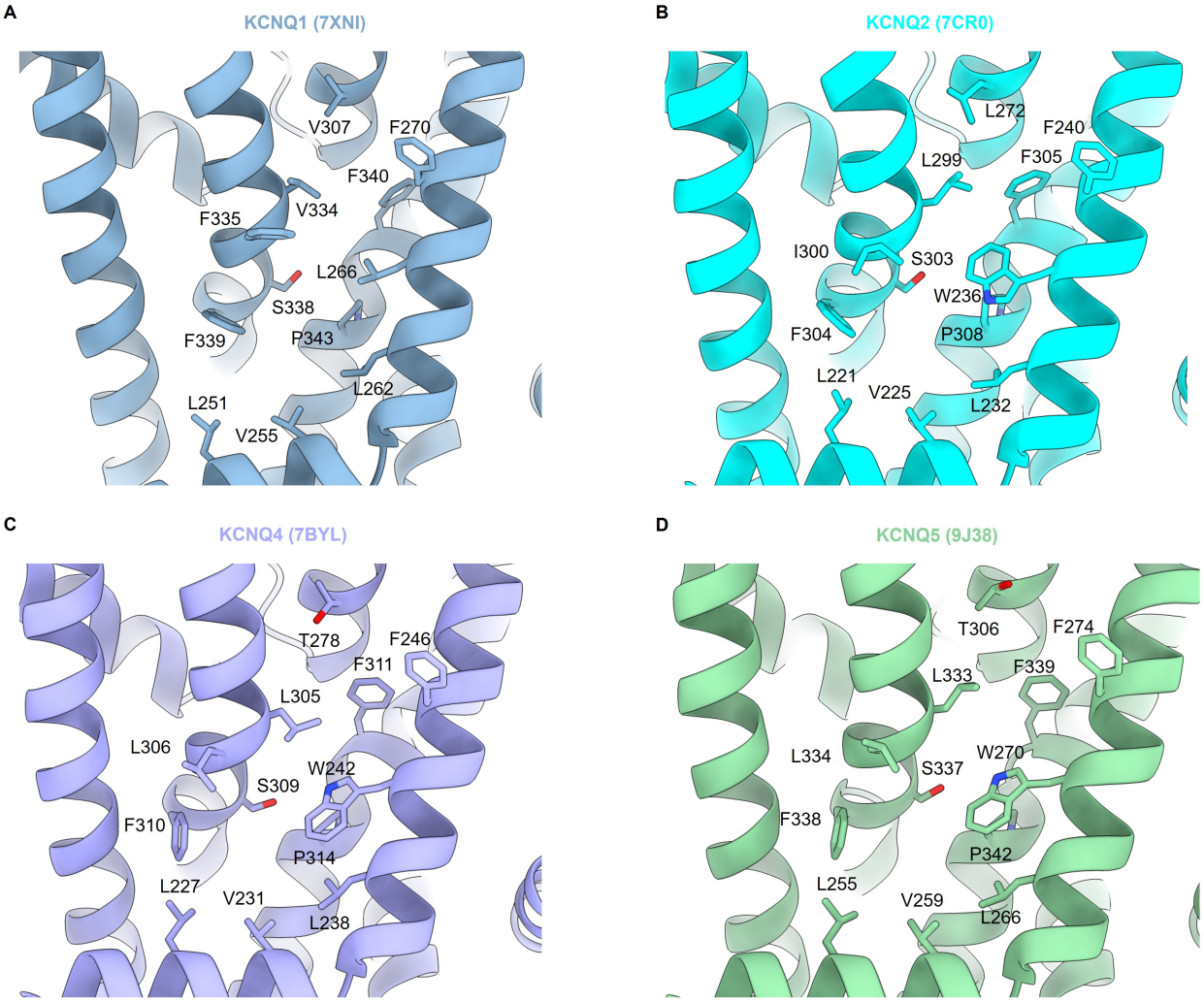

E

KCNQ2	F104	L221	V225	L232	W236	G239	F240	L243	L272	L299	I300	S303	F304	F305	P308	L312
KCNQ3	L134	L250	I254	L261	W265	G268	F269	L272	L311	L338	I339	S342	F343	F344	P347	L351
KCNQ1	L134	L251	V255	L262	L266	G269	F270	L273	V307	V334	F335	S338	F339	F340	P343	L347
KCNQ4	F110	L227	V231	L238	W242	G245	F246	L249	T278	L305	L306	S309	F310	F311	P314	L318
KCNQ5	F138	L255	V259	L266	W270	G273	F274	L277	T306	L333	L334	S337	F338	F339	P342	L346

Figure S6. The XEN1101 binding site in KCNQs. (A) Local magnified image of the XEN1101 binding site in KCNQ1 (7XNI) [53]. **(B)** Local magnified image of the XEN1101 binding site in KCNQ2 (7CR0) [26]. **(C)** Local magnified image of the XEN1101 binding site in KCNQ4 (7BYL)

814 [51]. **(D)** Local magnified image of the XEN1101 binding site in KCNQ5 (9J38) [48]. **(E)** Sequence
815 alignment results of all amino acids that may interact with XEN1101 in the binding pocket of
816 KCNQ1-5. Green marks indicate similar amino acids, red marks indicate non-conserved amino
817 acids, and identical amino acids are not marked.
818
819

820 **Table S1. Cryo-EM data collection, refinement and validation statistics.**

Structure	$KCNQ2/3_{apo}$	KCNQ2/3-XEN1101-PIP_2
EMDB accession code	EMDB-66589	EMDB-66607
PDB accession code	9X5J	9X65
Data collection and processing		
Magnification	130,000	130,000
Voltage (kV)	300	300
Electron exposure (e–/Å^2)	50.44	50.52
Defocus range (μm)	-1.0 ~ -2.0	-1.0 ~ -2.0
Pixel size (Å)	0.891	0.891
Symmetry imposed	*C1*	*C1*
Initial particle images (#)	7,366,139	5,233,817
Final particle images (#)	217,315	131,114
Map resolution (Å)	3.05	3.19
FSC threshold	0.143	0.143
Refinement		
Initial model used (PDB code)	AlphaFold-KCNQ3, 7CR3	9X5J (this paper)
Model resolution (Å)	3.60	3.05
FSC threshold	0.143	0.143
Model composition		
Non-hydrogen atoms	15,300	15,192
Protein residues	1900	1864
Ligands	4	11
***B* factors (Å^2)**		
Protein	44.06	51.80
Ligand	32.44	13.57
r.m.s. deviations		
Bond lengths (Å)	0.004	0.004
Bond angles (°)	0.586	0.597
Validation		
MolProbity score	1.71	1.64
Clashscore	12.44	12.93
Poor rotamers (%)	0.12	0.13
Ramachandran plot		
Favored (%)	97.47	97.92
Allowed (%)	2.53	2.08
Disallowed (%)	0.00	0.00

821